THESIS FOR THE DEGREE OF LICENTIATE OF ENGINEERING

Radiative transfer models for rotary kilns – from fossil fuels to hydrogen gas and thermal plasmas

ELIAS EHLMÉ

Department of Space, Earth, and Environment

CHALMERS UNIVERSITY OF TECHNOLOGY

Gothenburg, Sweden 2025

Radiative transfer models for rotary kilns – from fossil fuels to hydrogen gas and thermal plasmas
ELIAS EHLMÉ

Department of Space, Earth, and Environment
Chalmers University of Technology
SE-412 96 Gothenburg
Sweden
Telephone + 46 (0)31-772 1000

Printed by Chalmers Reproservice
Gothenburg, Sweden 2025

Radiative transfer models for rotary kilns – from fossil fuels to hydrogen gas and thermal plasmas

ELIAS EHLMÉ

Division of Energy Technology

Department of Space, Earth, and Environment

Chalmers University of Technology

Abstract

Global warming caused by greenhouse gas emissions remains a serious challenge in our Society. Combustion of fossil-based fuels is common in thermal engineering processes within the industrial sector. Electrification of such processes is key to reducing related carbon dioxide and particle emissions. Industries that are aiming to electrify by adapting current processes to operate with alternative fuels, such as hydrogen gas or thermal plasmas, require a comprehensive understanding of the combustion processes, heat transfer mechanism, overall heat balances, and process optimization. Therefore, there is an urgent need to develop modeling tools and to conduct experiments to validate those tools.

This thesis investigates the effects on the heat transfer within rotating furnaces that occur when substituting fossil-based fuels for alternatives, such as hydrogen gas and electrically aided heating using thermal plasmas. The focus is on radiative heat transfer assessed in rotary kiln processes (high-temperature processes) that are used for iron ore and cement production.

Paper I present a heat transfer modeling study employing adiabatic flame temperature conditions, showing that the fuel shift from coal to hydrogen gas in rotary kilns for iron ore production significantly increases the local heat transfer rate to the inner surface of the kiln wall. Specifically, the heat transfer rate is affected near the burner region, achieving high levels for the hydrogen flame. Further investigations of the local effects of fuel shifting in rotary kilns require precision in terms of the heat transfer calculations, motivating the development of an updated gas radiation model, as presented in **Paper II**, and the application of such gas radiation models with computational fluid dynamics codes, as presented in **Paper III**.

By combining computational fluid dynamics codes with the updated gas radiation model, the present work concludes that, although using hydrogen gas as a fuel effectively reduces carbon dioxide emissions and particle formation, heat transfer during hydrogen firing is less efficient than during coal firing. Consequently, most of the heat transferred from fuel heat release exits with the flue gases during hydrogen combustion due to increased flame temperatures. This indicates a need for either coal-hydrogen co-firing conditions, as the presence of particles may enhance effectively the heat transfer rate within the kiln or alternative kiln designs.

Keywords: Radiative heat transfer, rotary kilns, hydrogen, thermal plasma

List of Publications

This thesis includes the following papers, which are referred to in the text by their Roman numeral:

I E. Ehlmé, A. Gunnarsson, K. Andersson, F. Normann, *Heat Transfer Conditions in Hydrogen-Fired Rotary Kilns for Iron Ore Processing. Ind. Eng. Chem. Res.* **2023,** 62: 15098-15108.

II E. Ehlmé, A. Gunnarsson, F. Normann, K. Andersson, *Updated Weighted-Sum-of-Gray-Gases Model Parameters for a Wide Range of Water and Carbon Dioxide Concentrations and Temperatures up to 5000 K. ACS Omega* **2025,** 10: 2978-2985.

III E. Ehlmé, A. Gunnarsson, F. Normann, K. Andersson, *An Assessment of Weighted-Sum-of-Grey-Gases Models for Computational Fluid Dynamics Modeling of Hydrogen Flames and Thermal Plasmas in Kilns. To be submitted* **2025.**

Authors' contributions
Elias Ehlmé is the main author of **Papers I II** and **III**, responsible for the modeling and method development, and the writing of the papers. Assistant Professor Adrian Gunnarsson has contributed with modeling supervision and resources (3D heat transfer modeling tool), discussions, writing, and editing. Professor Fredrik Normann and Professor Klas Andersson have contributed with discussions, writing, and editing. Dr. Ehsan Fooladgar has contributed to **Paper III** with computational fluid dynamics modeling, discussions, and editing.

Acknowledgments

I would like to start by thanking my supervisors Adrian Gunnarsson, Fredrik Normann, and Klas Andersson for their commitment and contributions to the work and their constant support. Your guidance has not only shaped this work, but also created a creative and inspiring environment that has kept me continuously motivated. Thank you for our progress meetings; I am deeply grateful for the time, input, and discussions from your knowledgeable perspectives. Thank you for the opportunity to do my Master's and PhD theses within this group and in such an exciting research field. Adrian, I have learned a lot from you in the process during these years and I know that I will continue to do so, thank you.

To my fellow colleagues and PhD students in the High-Temperature Processes research group, thank you for our discussions regarding cameras, thermal radiation, rotary kilns, and of course, modeling. I look forward to continuing our teamwork!

To the Magic group, thank you for our gaming nights, accompanied by burgers, competitions, and laughs.

To my wonderful parents, brothers and friends, thank you for reminding me to take breaks, for our past adventures, and for the many more adventures to come. Finally, to Maria, thank you for your unwavering support throughout the years that we have spent together.

LKAB and the Swedish Energy Agency are acknowledged for the financial support of this work.

Elias Ehlmé

Gothenburg, Sweden

March, 2025

Table of Contents

Outline

This thesis includes a summary of the work and the three appended papers. The first three chapters describe the background to the topics of the thesis, related previous work, and thermal radiation theory. Chapter 4 describes the heat transfer model, which is an essential tool within this work, the modeling setup, and the discrete transfer model. Chapter 5 compares the results of **Papers I** and **III**, showing the improvements to the modeling work from **Paper I**. Finally, Chapters 6 and 7 present the conclusions from the thesis and provide possible directions for future work.

Paper I assesses the heat transfer conditions with the focus on radiative transfer via a kiln-based heat transfer model, which represents the rotary kilns used in heat treatment processes for iron ore production. The modeling study implements adiabatic flame conditions to model coal-fired and hydrogen-fired kilns, and compares the heat transfer contributions to the kiln surfaces. Two areas of improvement with respect to the heat transfer study are identified and addressed in **Papers II** and **III**.

In **Paper II**, updated gas radiation parameters for use in a weighted-sum-of-gray-gases model (WSGGM) are generated and evaluated, extending the applicable range up to 5000 K, which is suitable for modeling hydrogen combustion and plasma-heated systems. The evaluation focuses on 1D homogeneous/non-homogeneous and isothermal/non-isothermal gaseous domains, assessing the accuracy levels against a statistical narrow-band model used as the reference.

Paper III compares the WSGGM of **Paper II** with models applied in computational fluid dynamic codes, assessing the relevant gas radiation approaches in three cases defined by the kiln-based heat transfer model: coal-fired; hydrogen-fired; and thermal plasma-heated kilns.

1. Introduction

The impact of global warming caused by greenhouse gases remains a crucial challenge for modern Society. Substantial amounts of greenhouse gases are produced during the combustion of fossil fuels, specifically in the transportation sector and in industries, such as those involving thermal engineering processes and power generation. During combustion, air is typically used as oxidant, resulting in flue gases that contain chemical compounds, mainly water vapor, nitrogen, and carbon dioxide. Moreover, the combustion is often incomplete, leading to the release of particulate matter in the forms of char, ash, and soot, especially from solid-based fossil fuels such as pulverized coal, which is valued for its availability, high heating value, and low cost, despite its negative environmental impacts.

To address these emissions, recent technological advancements have focused on capturing the carbon dioxide in the flue gas through absorption, as in the carbon capture storage (CCS) technology, and oxyfuel combustion, where air is replaced by oxygen, resulting in low nitrogen and high carbon dioxide concentrations, facilitating CCS. Alternatively, some advancements have focused on electrifying the existing processes through the utilization of decarbonized fuels. Substituting fossil-based fuels with electrification through alternative fuels – such as hydrogen gas or electrically aided combustion via thermal plasmas that apply a process-suitable working gas – can significantly reduce the levels of greenhouse gas emissions and particle formation. For instance, combusting hydrogen primarily produces flue gases that consist of water vapor. Hydrogen is considered a renewable fuel if produced from green energy sources, such as solar, wind or hydro power. Thermal plasma technologies may also be regarded as a renewable energy source if the required electricity is produced from green energy sources.

However, transitioning towards electrification through hydrogen gas or plasma technology requires a deep understanding of how these changes affect the heat transfer that occurs during combustion and material heat treatment. Heat transfer within high-temperature enclosures, such as furnaces, is primarily governed by the thermal radiation emitted from the fuel heat release. Accurately estimating radiative transfer is complicated, as it is affected by the presence of gases (particularly water vapor and carbon dioxide) and particles suspended in the flame, which absorb, emit, and scatter the radiation in the furnace. Thus, adapting combustion processes requires knowledge of chemistry, fluid dynamics, and thermal radiation, assessed through combinations of measurements and modeling tools.

1.1 Aim

This work aims to develop heat transfer models, with the focus on radiation, to study the effects on the overall and local heat transfer conditions within furnaces for the fuel shift from coal to hydrogen gas or thermal plasmas. The models can be employed in various modeling frameworks and for a wide range of applications. Here, the models are evaluated in cylindrical rotating furnaces, i.e., rotary kilns, used in high-temperature processes for iron ore and cement production. This thesis includes: heat transfer modeling studies of coal-fired, hydrogen-fired, and plasma-heated kilns; the generation of updated parameters for gas radiation modeling, and the application of gas radiation models in computational fluid dynamics (CFD) codes.

Scope

This thesis focuses exclusively on the kiln section within the respective high-temperature processes. As such, the heat that exits with the flue gases from the kilns and its effects on the respective overall process are considered outside the scope of this work.

Three models are examined, each with varying complexity in terms of radiative transfer calculations, depending on the selected sub-models:

- For three-dimensional problems, a heat transfer model with detailed descriptions of the heat transfer mechanisms (specifically for radiation) within the kilns and without mass or momentum transport equations. The heat transfer model offers the possibility to study the isolated effects on the kiln heat balance of temperature, gas, and particle profiles, which are defined as inputs.
- A three-dimensional computational fluid dynamics model, of limited complexity with respect to radiative transfer calculations but including heat, mass, and momentum transport equations to generate the flow field within kilns. Thus, the model can be used to provide detailed inputs to the heat transfer model.
- For one-dimensional problems, a discrete transfer model, which has the highest level of complexity with respect to radiative transfer calculations among the included models, examines local radiative transfer effects by comparing sub-models of varying complexity. The model allows for evaluations of selected sub-models to improve the precision of the radiative transfer calculations within the heat transfer model.

2. Background

The rotary kiln – a high-temperature process

The rotary kiln, which is a cylindrical rotating furnace for heat treatment of solid materials, is commonly used in industries such as iron ore processing, cement, and pulp and paper production [1–5]. An example of a process with a rotary kiln is the grate-kiln process, which is a high-temperature process used for iron ore production (Fig. 1). This process includes a grate section in which pretreated iron ore (here called 'green pellets') undergoes drying, preheating, and sintering in different zones (denoted as UDD to PH in Fig. 1), followed by heat treatment in the rotary kiln, and cooling with ambient air in a cooler (C1–C4 in Fig. 1) [4]. In the cooling unit, gases are recycled to provide heat to the grate zones.

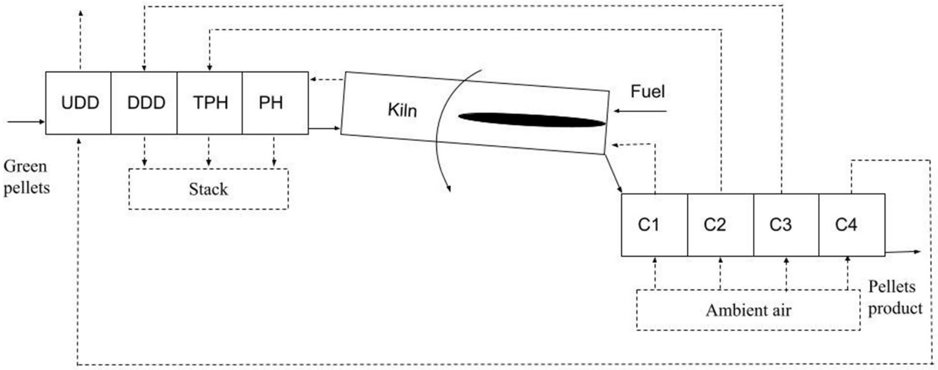

Figure 1: Schematic of a grate-kiln process: a high-temperature process for iron ore production. Source: ***Paper I****.*

Another example of a process with a rotary kiln is the high-temperature process used for cement production (Fig. 2). Here, the raw material is a pretreated raw meal, which undergoes preheating in a series of cyclones that are arranged in a tower (denoted Cy1–Cy5 in Fig. 2), followed by chemical transformation through calcination within the calciner [6]. The material undergoes further chemical transformation by heat treatment within the kiln. Finally, the product is cooled with air within the cooler, and the gases from the cooling unit are recycled as preheated air to the kiln and calciner.

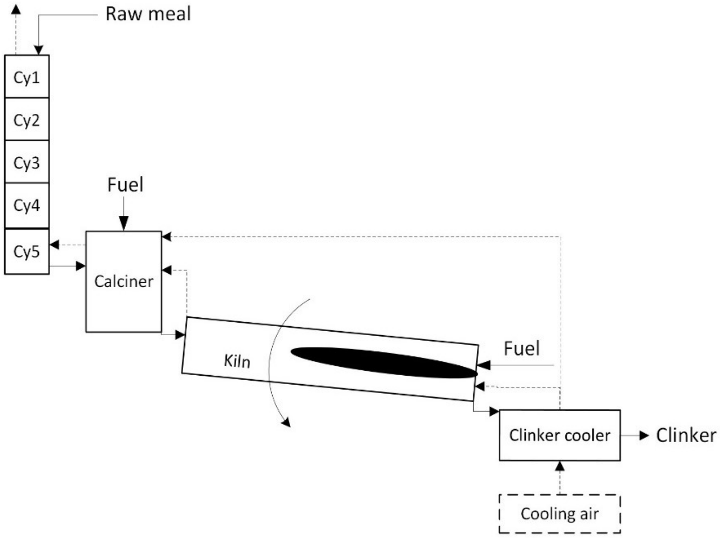

Figure 2: Schematic of a high-temperature process for cement production.

In direct-fired kilns, as shown in Figures 1 and 2, the burners at one end combust the fuel to supply heat, and the material entering in the opposite direction to the burner flows counter-currently to the flame. The majority of the heat transfer is by thermal radiation originating from the large luminous flame, which is typically fueled by pulverized coal/mixtures of fossil fuels and preheated air. Thus, large industries that continuously operate rotary kilns generate substantial carbon dioxide emissions, prompting industrial users to transition to less-carbon-intensive fuels or electrically aided heating. However, measuring and implementing process changes is challenging due to the complexity of the heat transfer to the kiln surfaces from the fuel heat release, which is influenced by radiation, convection, and conduction, as well as the rotation of the kiln.

Anticipated from the substitution of fossil-based fuels for electrification is the reduction of char, ash, and soot particles, components that have been shown to dominate the contribution to radiative transfer [7]. Therefore, substituting for electrification, through the use of hydrogen gas or thermal plasmas, is likely to decrease the overall heat transfer, since particle radiation effects are terminated. The transition is likely to result in a gas volume with higher peak temperatures and increased concentrations of water vapor (from hydrogen) or carbon dioxide (from thermal plasmas with carbon dioxide as the working gas), further enhancing the intensity of heat transfer, especially locally. It is, therefore, of interest to study how the fuel shift affects the overall and local heat transfer conditions within kilns by developing detailed modeling tools, as well as to identify new modeling strategies for treating the radiation of the changed gas volume.

Rotary kilns - heat transfer studies using alternative fuels

The rotation and size of the kiln complicate the takin of measurements during operation, and full-scale studies on substituting fossil-based fuels for alternative fuels are scarce. Therefore, some works have focused on developing models or conducting experiments on downscale stationary kilns [8–13]. However, few studies have focused on radiation. Previous work from our research group, includes the studies conducted by Gunnarsson et al. [8] and Bäckström et al. [9], who looked at various fuel combinations, such as coal and biomass, in 580-kW and 400-kW pilot-scale test furnaces to analyze the effects on temperature and radiative transfer. Their results revealed the possibility to model the radiative transfer for such combustion conditions, and that particle radiation dominated the heat transfer from the tested flames. Johansson et al. [10] examined coal and hydrogen co-firing conditions with different burner designs in a 130-kW furnace and their effects on NO_x emissions. Their study showed that radiative heat transfer dominated, with co-firing (70% coal and 30% hydrogen) generating a more-intense flame, enhanced peak flame temperatures and heat transfer, specifically near the burner region, as compared to pure coal combustion.

A deeper understanding of the heat transfer within kilns is achieved through advanced modeling approaches, particularly for modeling thermal radiation [1,3,5,7,14–18]. However, accurately assessing radiation is complex, as it requires the selection of appropriate models and strategies based on the complexity of the problem. Methods for treating radiation can be found in the work of Modest [19]; many of these methods have been used in our research group to develop models for studying radiation within cylindrical enclosures [20] [21]. The methods often require the integration of sub-models to determine how a radiative path is affected by the presence of gases and/or particles. In recent years, these sub-models, specifically for gas radiation, have been updated frequently to suit diverse combustion conditions, e.g., oxyfuel, oxygen-enriched, gasification, and hydrogen combustion [17–27]. Many of these are based on the original models developed by Hottel and Sarofim [33] (weighted-sum-of-gray-gases models), Edwards [34], Modak [35], Lallemant [36] (exponential wide-band models), and Leckner [37] (Leckner model).

Our research group has combined detailed radiation modeling with other heat transfer mechanisms to model the heat transfer within kilns by developing a 3D heat transfer modeling tool [21]. However, this tool does not include sub-models for chemistry or fluid dynamics. Coupling radiation modeling with chemistry and fluid dynamics for heat transfer calculations within kilns requires more-complex modeling frameworks, such as CFD codes. However, these CFD frameworks are usually limited in terms of the complexity of the radiative transfer calculations. Nonetheless, the usage of CFD codes as a modeling framework has lately gained substantial attention in the scientific community. Fooladgar et al. [11] have combined CFD and experiments to study NO_x formation in a pilot-scale furnace that represents a kiln that uses a plasma torch and applying air, pure N_2, and mixtures of H_2 and N_2 as plasma-forming gas. Their study shows the possibilities for using H_2 and N_2 as a plasma-forming gas, reaching the same order of NO_x formation as traditional fossil fuels. Hercog et al. [12] have applied CFD modeling to study the heat transfer effects on burners in cement kilns during petroleum coke and hydrogen co-firing. Here, it is shown that adding hydrogen to the fuel mixture increases the peak flame temperatures, thereby improving heat transfer locally, which may damage the inner kiln wall close to the burner. Wang et al. [13] have studied the effects of combustion using mixtures of hydrogen and propane gas for the design and operating conditions of rotary kiln burners. Their work shows that mixing hydrogen with propane while maintaining the same total heat release can effectively reduce the levels of carbon oxides and NO_x emissions.

In summary, these studies highlight the importance of implementing advanced modeling tools, as well as experimental data, to study/optimize heat transfer, flame characteristics, and NO_x emissions during the transition to electrification using alternative fuels in kilns.

3. Radiation – Governing equations and theory

The radiative heat transfer equation (RTE), as expressed in Eq. (1), describes the radiative intensity change for a given wavenumber in a set direction, s, which depends on the participating gases and particles in a ray's path as they absorb, emit, and scatter radiation. The absorption coefficient, κ_v, depends on the radiative properties of the present gases and particles, while the scattering coefficient, σ_s, and the scattered intensity in a set direction, described by the integral term, depend on the present particles only.

$$\frac{dI_v}{ds} = \kappa_v I_{bv} - (\kappa_v + \sigma_{sv}) I_v + \sigma_{sv}/4\pi \int_0^{4\pi} I_v(\hat{s}_i) \Phi_v(\hat{s}_i, \hat{s}) d\Omega_i \tag{1}$$

Discrete transfer model and discrete ordinates method

This work applies two modeling approaches to calculate the radiative intensity field: the discrete transfer model (DTM); and the discrete ordinates method (DOM). Both approaches employ *SN* approximation and discrete ordinates to define the ray's path through a domain. Along a radiative path, the spectral intensity, as given by the RTE, i.e., Eq. (1), is considered by a set of discrete directions called 'ordinates', each of which is paired with quadrature weights, which in total corresponds to the angle range 4π. The ordinates, μ, η, ξ, are illustrated in Figure 3, showing the intensity, I, at position (*x, y, z*) in the discrete direction $\Omega_m(\mu_m = \cos\Phi, \eta_m = \sin\Theta \sin\Phi, \xi_m = \sin\Theta \cos\Phi)$. Figure 3 also includes the sum over the total number of discrete directions, *N*, multiplying each ordinate by its corresponding weight, *w*. The ordinates and weights used in this work are obtained from Modest [19].

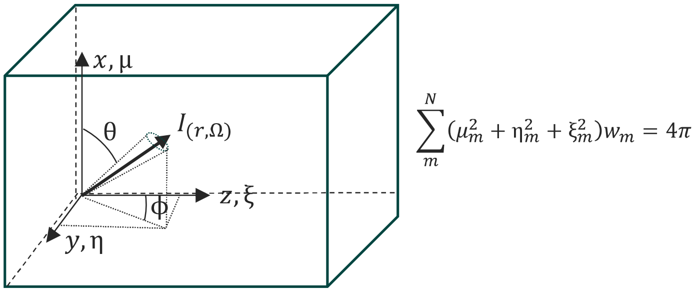

Figure 3: Direction cosines and coordinates.

For both the DTM and DOM, the radiative intensity is approximated along each ordinate, significantly reducing the number of radiative paths that need to be solved. The DTM traces each radiative path from a source of origin, solving the RTE along the path through the computational domain. In previous studies conducted by our research group, the DTM was applied to model the radiative intensity field, for instance, in oxyfuel combustion studies of an infinitely long cylinder by Johansson et al. [38] and in studies of radiative transfer of different fuel combinations in pilot-scale test furnaces by Gunnarsson et al. [8] and Bäckström et al. [9]. From their modeling work, the results comparing the measured intensity data and the intensities predicted by the DTM showed good accordance.

However, the ray tracing methods used in the DTM become cumbersome in a 3D geometry. Our group has, therefore, developed a DOM-based model of the radiative intensity field in a 3D cylindrical furnace, as presented in the paper of Gunnarsson et al. [20] [21]. The DOM divides a cylindrical enclosure into computational cells in the axial, radial, and angular directions, solving the RTE along each set of ordinates with its corresponding cells. In [21], the predictive capabilities of the DOM-based model, assessed by predicting the inner surface temperatures of a pilot-scale test furnace, were compared with the experimentally gathered data. The model showed an error of 11%, which is considered satisfactory.

In this thesis, the DOM is used to study the heat transfer conditions within 3D full-scale rotary kilns for various fuels. In addition, the DTM is employed to solve the radiative field in 1D slabs, allowing for evaluations of new gas radiation modeling parameters. The DTM is also used to investigate the local radiative transfer effects in a representative cross-section of the kiln, which is modeled as a gaseous domain located between two infinite black plates.

3.1 Radiative properties of gases

If no particles are present, the scattering coefficient, σ_s, in the RTE can be neglected, and the RTE is simplified according to Eq. (2). According to Eq. (2), the change in radiative intensity in a set direction can be calculated with the radiative properties of the present gases integrated over all wavenumbers. However, these properties depend on the temperature and species concentrations, requiring highly detailed knowledge of every spectral line for each species. Therefore, estimating the radiative properties of radiating gases that are typically found in combustion, such as H_2O and CO_2, requires models of lower complexity and decreased accuracy.

$$\frac{dI_\nu}{ds} = \kappa_\nu (I_{b\nu} - I_\nu) \tag{2}$$

Line-by-line and band models

Line-by-line (LBL) models, which integrate the RTE across multiple spectral lines in the gas spectrum, require information on the line strengths and the broadening of these lines, parameters that are dependent upon the temperature, gas concentration, and the pressure levels of the gases along a ray's path [19]. As such, a significant amount of data is required, and this can be gathered from spectroscopy databases. Some examples of these databases utilized across various fields, such as astrophysics, chemistry, and radiation, are: HITRAN1996, HITRAN2004, HITRAN2008, and HITRAN2010, with molecular data for temperatures up to 3000 K; and HITEMP and HITEMP2010 with data for temperatures up to 5000 K [39–44].

Other models are based on statistical bands that divide the gas spectrum into wide or narrow spectral bands, representing a range of wavelengths that contain many spectral lines [19]. Within these bands, the spectral properties are treated as constant, resulting in statistically averaged gas properties for each band. These models often require tabulated band parameters for the gas, which are derived from the HITRAN/HITEMP databases and can be found in the reports from the EM2C lab [45–47] (based on the HITRAN1992 database, with additional spectral lines from Flaud et al. [48]) or the updated parameters from the work of Rivière et al. [49].

Since the performance levels of the models depend on the spectroscopy database used, Chu et al. [50] and Becher et al. [51] have compared the different spectroscopy databases. In the study of Chu et al. [50], an LBL model using the HITEMP1995, HITRAN2004, HITRAN2008, and HITEMP2010 databases was compared against a statistical narrow-band model (SNBM) using the EMC2 lab band parameters. The analysis focused on radiative transfer calculations for H_2O and CO_2, as well as the mixture of the two. Their results showed that older databases are missing many hot-lines at higher temperatures, specifically beyond 1000 K. In addition, the SNBM was found to perform as accurately as the LBL model for the studied cases. In both [50] and [51], it was concluded that HITEMP2010 is the preferred database.

Moreover, the exponential wide-band model (EWBM) [34] [52] [53], which is similar to the statistical band models, assumes that gas absorption occurs in spectral bands. It employs average band parameters over a specified wavenumber interval that varies with temperature and wavenumber over the band. Here, the band parameters are approximated using analytical expressions, requiring a smaller database compared to the SNBM and LBL model [36]. However, the EWBM has demonstrated limited accuracy in terms of producing the total emissivity of gases, such as for mixtures of H_2O and CO_2; see [54] [55]. Furthermore, the described band models (SNBM and EWBM) are currently limited to predicting the radiant properties of gases only in the infrared (IR) spectra, specifically for wavenumbers relevant to thermal radiation, in the range of 50–11250 cm^{-1}. The emission and absorption events in the IR spectra are mainly due to the changes in the vibrational states of the gas molecule, whereas the emissions in the UV-to-visible spectra are due to excitation within the molecule [36]. Thus, the descriptions of these transitions differ, and new expressions have yet to be derived.

Global models

The most-efficient models for estimating the radiative properties of gases, in terms of computational effort, are global models that consider the entire gas spectrum with absorption coefficients. These models aim to fit the radiative data of gas species within a range of temperatures, gas mixtures, and pressure-path lengths [36]. The simplest of these models are the gray gas models, which assume that the absorption coefficient of the gas medium is constant across all wavelengths. Typically, a spectrally averaged coefficient is used.

The weighted-sum-of-gray-gases model (WSGGM) is widely used in engineering applications. The model treats the spectrum as one in which gases participate in radiation through a set of gray fictitious gases, each represented by an absorption coefficient and corresponding weight [33]. It can be employed as a gray gas model or to model non-gray gas behavior by estimating various gray gases that represent spectral absorption coefficients within the gas spectrum. The WSGGM is used in particular to model H_2O and CO_2 species, whereas the LBL and band models can be used to model a variety of species. The accuracy of the WSGGM depends on: (i) the accuracy of the radiative database that the model aims to fit; and (ii) the fitting process used to minimize the numerical differences between the model and the database. Consequently, the model's accuracy depends on the range of data that it must cover, which is a limitation. As a result, many different WSGGM parameters have been developed to suit specific conditions [17–27].

Other methods that apply absorption coefficients to model the non-gray gas behavior reorder the absorption lines on the wavenumber spectrum. These include the full-spectrum *k*-distribution (FSCK) model [56] [57], the spectral-line-based weighted-sum-of-gray-gases (SLW) model [58] [59], and the absorption distribution function (ADF) approach [60]. The SLW model is similar to the WSGGM except that it utilizes line-by-line databases to calculate the weight factors. In contrast, the ADF approach is similar to the SLW model but differs with respect to how the weights are calculated. The FSCK model assumes a spectrally reordered absorption coefficient over a narrow-band, part-spectrum or the full-spectrum by integrating over the Planck-weighted function [56]. The result is a continuous *k*-distribution and contrasts with the WSGGM, SLW, and ADF models, which generate step-wise absorption coefficients (see Fig. 4). However, application of the FSCK model to radiative transfer calculations is limited, since the correlations are provided for only one gas species. Including multiple gas species requires one to combine the spectra of the various species, which is difficult to approximate as it includes determining the *k*-distribution of the mixture from the *k*-distribution of each individual gas species. As such, two mixing models have been proposed: the multiplication model [57]; and the un-correlated mixture model [61].

The LBL and narrow-band models are the most-accurate models for predicting the radiative properties of absorbing and emitting gases. However, since they require large amounts of data, using them in radiative transfer problems becomes too expensive computationally. As a result, these models are often employed in simple geometries to provide a benchmark solution for evaluating other gas radiation models, such as the WSGGM. The differences in complexity between the three gas models, LBL, SNBM, and WSGG, are illustrated in Figure 4.

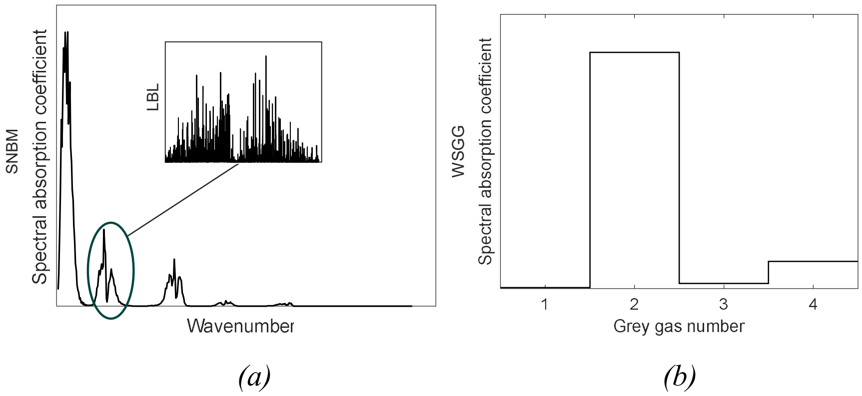

(a) *(b)*

Figure 4: Examples of the spectral absorption coefficients estimated by an SNBM, including an example of the LBL model (a), and the WSGGM showing one clear and three gray gases (b).

This thesis employs two of the mentioned gas radiation models. It includes the WSGGM, due to its simplicity and efficiency of use in complex heat transfer problems. In specific cases, the statistical narrow-band model (SNBM) is used for its high level of accuracy in evaluating less-complex problems.

Weighted-sum-of-gray-gases model

The WSGGM, originally proposed by Hottel and Sarofim [33], has previously been updated to suit specific combustion conditions [17–27]. In this context, our research group [23] has updated the WSGGM parameters described in [33] to suit oxy-fuel combustion. In the work of Johansson et al. [23], the accuracy of the model was assessed through radiative source term test cases in a 1D slab that consisted of a gaseous domain with two infinite black plates. Specifically, to evaluate the WSGGM accuracy, a DTM (see [38]) was employed to solve the radiative heat transfer equation under isothermal non-homogenous and non-isothermal homogeneous/non-homogeneous conditions. In this work, a similar method is applied to generate and assess the accuracy of the updated WSGGM parameters presented in **Paper II**.

Calculating the total emissivity using the WSGGM, as in Eq. (3), requires, for each gray gas, j, the corresponding weight, a_j, and absorption coefficient, κ_j, as well as the pathlength, S, pressure P, and molar fraction, Y. Equation (3) also includes one clear gas, where the total number of gray gases and the clear gas sums to J.

$$\varepsilon_{WSGG} = \sum_{j=1}^{J} a_j\left(1 - exp\left[-\kappa_j SP\left(Y_{CO_2} + Y_{H_2O}\right)\right]\right) \tag{3}$$

The weight of each gray gas, a_j, is expressed in Eq. (4) as a function of temperature and represents the fraction of the black-body radiation for spectral regions in which a gray gas with absorption coefficient κ_j exists. The absorption coefficient of the clear gas is set to zero, to account for all the transparent windows between the absorption bands. The sum of all the weights (including the clear gas) is unity, and the reference temperature is constant and is dependent upon the applied WSGGM.

$$a_j = \sum_{i=1}^{I} c_{j,i}\left(T/T_{ref}\right)^{i-1} \tag{4}$$

In more recent models, the coefficients κ_j and $c_{j,i}$ of each gray gas are polynomial functions of the molar ratio of water vapor and carbon dioxide, MR, and its polynomial degree can vary depending on the WSGGM. Expressed in Eq. (5) is an example of a four-order polynomial, which is used in the model presented in **Paper II**, and the coefficients $C1 - C5$ and $K1 - K5$ are all constants for each gray gas, as listed in **Paper II**.

$$\begin{gathered} c_{j,i} = C1_{j,i} + C2_{j,i}\left(\frac{Y_{H_2O}}{Y_{CO_2}}\right) + C3_{j,i}\left(\frac{Y_{H_2O}}{Y_{CO_2}}\right)^2 + C4_{j,i}\left(\frac{Y_{H_2O}}{Y_{CO_2}}\right)^3 + C5_{j,i}\left(\frac{Y_{H_2O}}{Y_{CO_2}}\right)^4 \\ \kappa_j = K1_j + K2_j\left(\frac{Y_{H_2O}}{Y_{CO_2}}\right) + K3_j\left(\frac{Y_{H_2O}}{Y_{CO_2}}\right)^2 + K4_j\left(\frac{Y_{H_2O}}{Y_{CO_2}}\right)^3 + K5_j\left(\frac{Y_{H_2O}}{Y_{CO_2}}\right)^4 \end{gathered} \tag{5}$$

Statistical narrow-band model

The SNBM statistically averages the radiative properties across spectral bands that represent a range of wavelengths over which the participating gases in a ray's path absorb and emit radiation. The SNBM used in this work applies the Malkmus model [62], as expressed in Eq. (6), for which the tabulated parameters for each band include the mean line-intensity to typical line-spacing within a narrow band, k_k, and the inverse of the mean line spacing, d_k, for the mean line half-widths, γ [45]. Here, the band parameters are gathered from previous work [49], and the parameters describing H_2O and CO_2 are based on spectroscopy databases. Specifically, the HITEMP 2010 database [44] is used for H_2O, while the CDSD-4000 database is used for CO_2 [63]. For detailed information on the accuracy of the mentioned spectroscopy databases, the reader is referred to the papers of Soufiani and Taine [45], Chu et al. [50], and Becher et al. [51].

In this work, the wavenumbers are defined for H_2O and CO_2 gases in the IR spectra, in the range of 50–11250 cm^{-1} with a spectral width of 25 cm^{-1}, resulting in a total of 449 bands. To address non-uniform pathways, the SNBM employs the Curtis-Godson approximation [19] [64].

$$\bar{\tau}_{v_k} = exp\left[-2\gamma\,/d_k\left((1+YPSk_kd_k/\gamma)^{1/2}-1\right)\right] \tag{6}$$

The mean spectral line-half width for H_2O and CO_2 used in Eq. (6) is temperature-dependent and determined according to Eq. (7). The reference temperature and pressure are 296 K and 1 atm, respectively. For H_2O and CO_2 mixtures, the total transmissivity of the gas mixture is the product of the transmissivities of the separate gases.

$$\begin{gathered}\gamma_{H2O} = \frac{P}{P_{ref}}\left\{0.462Y_{H2O}\frac{T_{ref}}{T} + \frac{T_{ref}}{T}^{0.5}[0.079(1-Y_{CO2}-Y_{O2}) + 0.106Y_{CO2} + 0.036Y_{O2}]\right\}\\ \gamma_{CO2} = \frac{P}{P_{ref}}\left\{\frac{T_{ref}}{T}^{0.7}\{0.07Y_{CO2} + 0.058(1-Y_{CO2}-Y_{H2O}) + 0.1Y_{H2O}\}\right\}\end{gathered} \tag{7}$$

Eq. (8) describes the total emissivity calculated by the SNBM using the averaged black-body intensity of band k (estimated from Planck's radiation law) and its corresponding transmissivity as in Eq. (6).

$$\varepsilon_{SNBM} = 1 - 1/I_b\sum_k \bar{I}_{bv_k}\bar{\tau}_{v_k} \tag{8}$$

Generation of WSGGM parameters

WSGGM parameters are generated using a predefined emissivity database, defined for a specific set of temperatures, pressure pathlengths, and species concentrations for each band or spectral line. This process involves using the LBL models that utilize HITRAN for spectroscopy data on the gases of interest or employing an SNBM with the band parameters for the gas species. Within this thesis, the SNBM approach is applied to construct an emissivity database, using Eq. (8) for pure H_2O and CO_2 species, as well as the mixture of the two, at temperatures up to 5000 K.

The WSGGM is then fitted to the database by minimizing the numerical difference between Eq. (3) and Eq. (8). The aim is to obtain, for each gray gas j, the weight parameters $c_{j,i}$, and absorption coefficient κ_j and their dependencies on concentration and temperature. Various numerical minimization methods can be applied. Here, the nonlinear least-squares method and the Levenberg-Marquardt algorithm [65] are used. These selected methods aim to fit polynomials that best represent the coefficients of κ_j and $c_{j,i}$ based on the reference emissivity.

Specifically, κ_j and $c_{j,i}$ can, for each gas concentration value Y (defined as either Y_{H2O}, Y_{CO2} or MR), be treated as equations for a 3D plane that describes the emissivity, temperature, and pressure pathlengths multiplied by the gas concentration, along the *z*-, *y*-, and *x*-axes, respectively. This is illustrated in Figure 5.

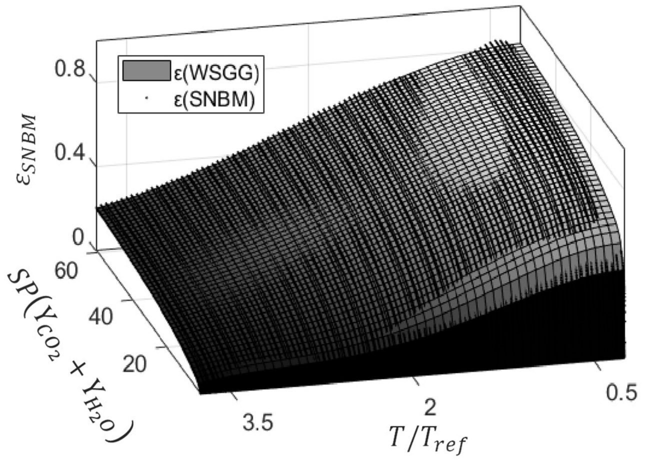

Figure 5: Example of a plane described by WSGGM parameters, which is fitted to the emissivity values calculated by the SNBM (dots).

In the following sequence, specifically for H_2O and CO_2 mixtures, the coefficients K and C from Eq. (5) are fitted to the sets of κ_j and $c_{j,i}$ coefficients through a second polynomial fit. Single H_2O and CO_2 species do not depend on the gas mixture fraction of Eq. (5), and only the sets of κ_j and $c_{j,i}$ coefficients are provided. All the coefficients needed for the updated WSGGM are listed in **Paper II**.

A summary of the overall minimization procedure applied for generating the parameters presented in **Paper II** is illustrated as a flowchart in Figure 6. Here, an iteration procedure is utilized to find the optimal fit and the iteration is divided into four steps, facilitating the fitting process by fitting the κ_j and $c_{j,i}$ coefficients for one gray gas at a time. Initially, a 3D plane is described with one gray gas, i.e., only four coefficients. In the next step, the known four coefficients are inputs to fit κ_j and $c_{j,i}$ for two gray gases, such that the coefficients are updated to achieve a more-precise fit. The iteration is repeated until the coefficients for all gas concentrations are defined.

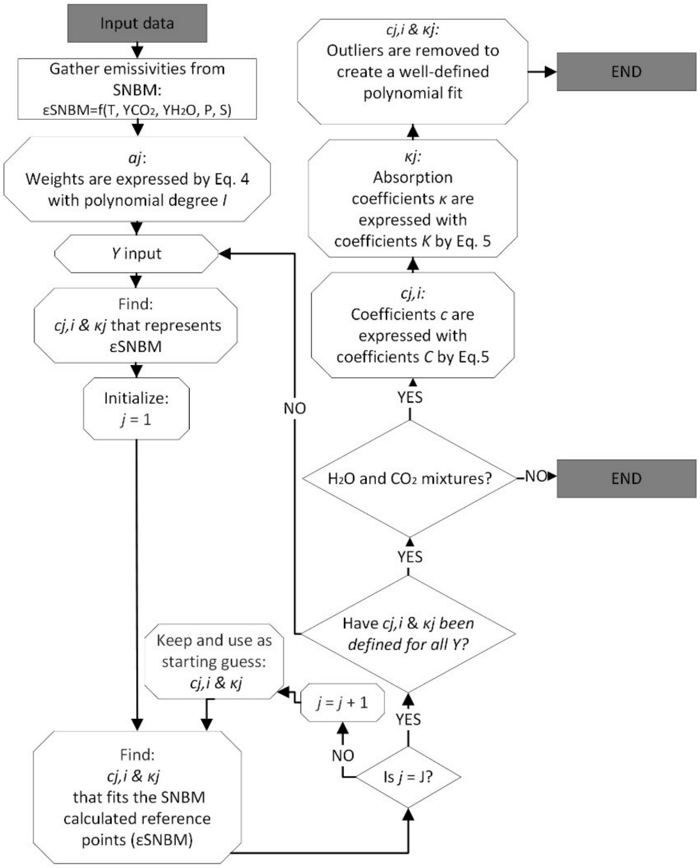

*Figure 6: Flowchart of the overall minimization procedure for defining coefficients for the weighted-sum-of-gray-gases model parameters presented in **Paper II**.*

3.2 Radiative transfer by gases

Integrating the RTE, as in Eq. (2), over the spatial domain and using the WSGGM or SNBM to estimate the radiative properties of gases give the discretized formulation, according to Eq. 9. Specifically, the radiative path is discretized into computational cells, solving the intensity for one homogeneous cell at a time evaluated over a spectral band k. Here, Eq. (9) is presented in terms of transmissivity, representing a radiative path as the sum of the difference in transmitted intensity multiplied by the spectral black-body intensity, $\bar{I}_{bv_k}$, of the neighboring cell position n-1 to n (9a), or for cell position n to ni, including the distance between those positions (9b). Equation (9a), which is known as the non-correlated formulation of the RTE, requires less computational effort compared to Eq. (9b) due to the absence of the summation term, and it is commonly used in CFD frameworks. For global models that use absorption coefficients, multiple spectral peaks are lumped together, making them efficient to use with Eq. 9a. Here, the WSGGM is applied with Eq. (9a). In contrast, the correlated formulation of the RTE, i.e., Eq. (9b), predicts the averaged spectral properties over band k as a function of the pathlength and is suitable for use with the SNBM.

$$\bar{I}_{v_k,n} = \bar{I}_{v_k,n-1}\bar{\tau}_{v_k,n-1\to n} + \bar{I}_{bv_k,n-1/2}(1-\bar{\tau}_{v_k,n-1\to n}) \tag{9a}$$

$$\bar{I}_{v_k,n} = \bar{I}_{v_k0}\bar{\tau}_{v_k,0\rightarrow ni} + \sum_{i=0}^{n-1} \bar{I}_{bv_k,n+1/2}(\bar{\tau}_{v_k,n+1\rightarrow ni} - \bar{\tau}_{v_k,n\rightarrow ni}) \tag{9b}$$

The radiative properties may be assumed to be non-dependent on the wavenumber, v, treating the gases as a gray medium, which reduces the number of intensity equations that must be solved. Integrating the WSGGM can be used to calculate the intensity with Eq. (9), which results: for a non-gray gas, as in Eq. (10a); and for a gray gas, as in Eq. (10b). In Eq. (10a), the intensity is solved along its defined ordinate and corresponding computational cells for each gas *j,* and the total intensity is the sum of the intensities of each ordinate. For the gray gas, in Eq. (10b), the intensity is solved in a way similar to that shown in Eq. (10a), but instead a spectral averaged absorption coefficient, κ, is estimated by the WSGGM. The implication of assuming gray or non-gray gas properties was briefly investigated for oxy-fuel conditions by Johansson et al. [23], although the cases were limited to 1D problems. Their study concluded that a gray medium performs poorly when temperature gradients are present in the gaseous domains of H_2O and CO_2. Within this thesis, **Paper III** investigates the implications of a gray/non-gray gas assumption for 3D problems and its effect on the overall heat transfer for conditions relevant to coal/hydrogen combustion or plasma-aided heating.

$$I_n = \sum_{j=1}^{j} I_{j,n-1} exp\big[-\kappa_j(p_{H2O} + p_{CO2})\Delta s\big] + a_j I_{b,j,n-1/2}\big(1 - exp\big[-\kappa_j(p_{H2O} + p_{CO2})\Delta s\big]\big) \tag{10a}$$

$$\begin{gathered} I_n = I_{n-1}\exp\left(-\kappa\Delta s\right) + I_{b,n-1/2}(1 - \exp\left(-\kappa\Delta s\right)) \\ where\text{: } \kappa = -\ln(1 - \varepsilon_{WSGG}(T, Y, P, S_{char}))/S_{char} \end{gathered} \tag{10b}$$

In summary, calculating the total radiative transfer in a domain requires spectral integration, in order to yield the total intensities presented for a non-scattering medium by Eqs. (10a) and (10b). Applying a DTM or DOM to integrate further the total intensities over all solid angles, N, gives the radiative flux. As such, the incident radiative flux, q_r, is the sum of the intensities, *I*, weighted by a quadrature weight, ω_m, in a direction cosine, ζ, for a discrete direction, *m*, according to Eq. (11):

$$q_r'' = \sum_{m=1}^{N} I_m \omega_m \zeta_m \tag{11}$$

Similarly, the divergence of the radiative heat flux, q_r, which is the radiative source term, can for a 1D slab be calculated using Eq. (12). The source term is, for a radiative path and cell *n*, the difference between the locally absorbed and emitted intensities, I^+ and I^-, respectively. For the 1D slab, half of the ordinates originate from the wall at the beginning of a path, *n=0*, and the remaining half arise from the wall at the end of a path. In this thesis, the source term equation is solved by the DTM, providing information on the local radiative transfer effects for a specified gaseous domain.

$$\nabla q = \sum_{m=1}^{N/2} \omega_m \mu_m (I_n^+ - I_n^-) \tag{12}$$

3.3 Particles and gases in radiative transfer

Particle radiation

Incomplete combustion of solid-based fuels leads to the formation of particles, which are suspended in the flame and participate in radiation. Since the particles emit, absorb, and scatter radiation, the integral term of Eq. (1) must be modeled appropriately for radiative transfer calculations.

These particles continuously emit and absorb radiation in the spectrum and are characterized as broad-band emitters. Depending on their size, they can also scatter radiation via three distinct phenomena: diffraction, where the direction of a ray of light is changed due to the presence of particles; reflection; and refraction, where the light ray penetrates the particle and changes direction [19]. As such, the radiative scattering of light by a cloud of particles can be described in terms of the complex index of refraction and the size of the scattering particles, i.e., the ratio of the particle radius to the wavelength, at a given wavelength λ, according to Eq. (13):

$$\begin{aligned} m_\lambda &= n_\lambda - ik_\lambda \\ size &= \frac{2\pi\, radius}{\lambda} \end{aligned} \tag{13}$$

Equation (13) includes a real part, the refractive index n, and an imaginary part, the absorptive index k, which define the optical properties specific to the particle of interest. In this work, two types of particles are included for modeling the coal flames: fuel/char particles and soot particles, both of which are treated as spherical entities. In particular, the coal flames in **Paper I** include char and soot particles, whereas those in **Paper III** only include char particles.

The spectral dependency on the radiative properties is not as complex as that of gas radiation, although the modeling of particle radiation entails other challenges. As seen from the integral term in Eq. (1), solving the RTE in the presence of particles requires an absorption coefficient κ, scattering coefficient σ_s, and a scattering phase function Φ, representing the fraction of energy that is scattered from direction $\hat{s}_i$ into direction $\hat{s}$. Determining these parameters necessitates simplifications derived from sub-models. Typically, this requires information on particle composition, density, temperature, concentration, and size distribution [66]. The composition determines the refractive index.

A common assumption regarding heat transfer problems is isotropic scattering or non-scattering. Isotropic scattering assumes that the scattering of radiation is equal in all directions, i.e., the scattering phase function is equal to unity. For a non-scattering assumption, the scattering phase function is zero. However, other methods for estimating anisotropic scattering are also available, for instance, using a linear anisotropic phase function or a Delta-Eddington phase function [67].

Related to the scattering phase function is the forward scattering factor, f, which accounts for the amount of forward scattering such that a value of unity is treated as transmission. The absorption and scattering coefficients for a cloud of particles are related to f, such that an absorption, κ, and a scattering, σ_s, coefficient are calculated for a group of particles, i, as a function of the projected particle surface area, A_{proj}, particle emissivity, ε, and number density, N, as in Eq. (14). This approach is commonly applied in commercial CFD codes [67].

$$\begin{gathered}\kappa = \sum_i \varepsilon_{particle,i} N_i A_{proj,i} \\ \sigma_s = \sum_i (1 - f_i)(1 - \varepsilon_{particle,i}) N_i A_{proj,i}\end{gathered} \tag{14}$$

In the literature relevant to coal combustion modeling, a constant forward scattering factor, typically 0.6 or 0.9, is commonly used in conjunction with the assumption that the radiative particle properties are gray, neglecting the spectral dependency. As such, the particle emissivity is either constant at 0.9 or varies linearly between 1.0 and 0.6, representing the emissivities of unburnt coal and fly ash [68–71]. However, char and fly ash particles have significantly different scattering properties, since fly ash scatters more radiation and char tends to absorb more radiation [72]. Therefore, if both particle types are present in a flame, the radiative properties of coal and fly ash should be modeled separately with typical f and $\varepsilon_{particle}$ properties for the corresponding particle type and conditions.

Alternatively, f and $\varepsilon_{particle}$ can be replaced with the corresponding efficiency factors for absorption, Q_{abs}, and scattering, Q_{sca}, as in Eq. (15). Q_{abs} and Q_{sca} are functions of the optical particle properties determined from Mie theory. These properties can be either assumed as gray or non-gray, and their implications have been investigated [66].

$$\begin{gathered}\kappa = Q_{abs} A_{proj} \\ \sigma_s = Q_{sca} A_{proj}\end{gathered} \tag{15}$$

In this work, and as previously reported by Gunnarsson [20] [21], char particles are modeled by applying Mie theory using the functions of Mätzler [73], with the optical properties of particles from Foster and Howarth [74]. Part of the incoming radiation is scattered forward using a forward scattering factor of 0.8, as suggested by Gronarz et al. [75], while the remaining radiation is scattered isotropically. Fly ash particles are not considered in this work but can be included, for example, using the optical properties from Goodwin and Mitchner [76].

Soot particles

Since soot particles are smaller in size than char particles, they have a negligible effect on scattering, and their radiative properties can be estimated according to Rayleigh's theory [19]. Rayleigh's theory describes the particle radiation by soot particles through a spectral absorption coefficient, κ_v, which is a function of the particle volume fraction, f_f, and the complex refractive index $E(m_\lambda)$, according to Eq. (16):

$$\kappa_v = E(m_\lambda) \frac{6\pi f_f}{\lambda} \tag{16}$$

The function of the complex refractive index in Eq. (16) is spectrally dependent and has to be modeled. While several parameters are described in the literature, in this thesis, the needed spectral soot properties used during coal flame modeling are taken from the paper of Chang and Charalampopoulos [77].

Figure 7 illustrates the refraction index in Eq. (13) (Fig. 7a) and the absorptive index (Fig. 7b), on which both the spectral absorption and scattering coefficients of particles are based. Figure 7 includes char [74] and fly ash [76] particles, as well as soot [77]. As observed in Figure 7, the three particle types show distinct refractive and absorptive index behaviors across different wavelengths. In Figure 7a, char and soot particles show increasing refraction of light as a function of wavelength, whereas the fly ash particles are almost constant, showing wavelength dependency only in the narrow region of 6–13 μm. In Figure 7b, the absorption index for char and fly ash remains constant for most of the wavelengths, with spectral dependence seen only between 0.5 and 13 μm. In contrast, soot particles show an increasing absorption index with wavelength.

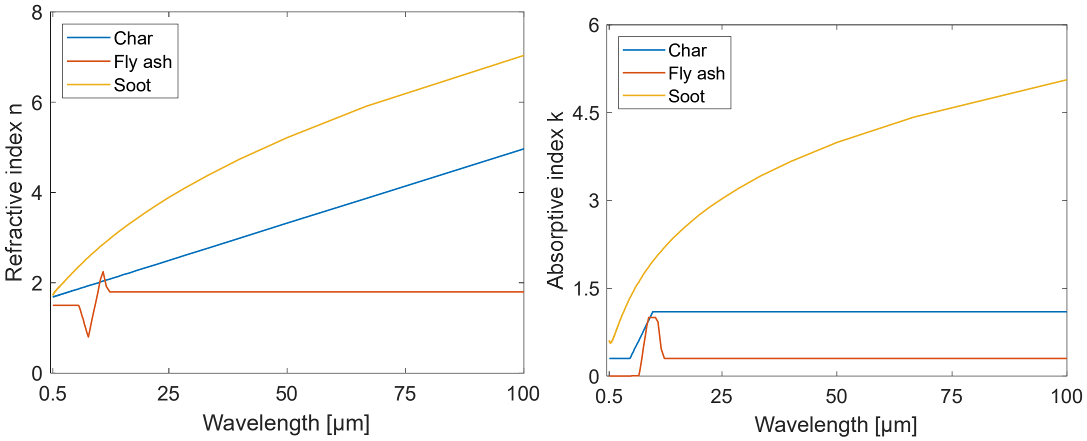

(a) *(b)*

Figure 7: Spectral variation of the refractive index and absorptive index parameters in Eq. (13) for coal, fly ash, and soot particles. The wavelengths are relevant for thermal radiation.

Particle and gas radiation

Determining the absorption coefficients for several particle types, such as char [Eq. (14) or Eq. (15)] and soot [Eq. (16)] particles, the summed radiative contribution is estimated from the sum of the absorption coefficients, as in Eq. (17):

$$\begin{gathered}\kappa_v = \kappa_{v,char} + \kappa_{v,soot} \\ \sigma_{s_v} = \sigma_{s_{v,char}}\end{gathered} \tag{17}$$

Furthermore, the effect of particle radiation on gas radiation can be determined by the total transmissivity over a spectral band, *k*, as expressed by Eq. (18), which is the product of the transmissivities of the gases and particles, estimated from the absorption and scattering coefficients. Equation (18) can be implemented with the SNBM.

$$\begin{gathered}\bar{\tau}_{v_k} = \bar{\tau}_{v_{k,gas}}\bar{\tau}_{v_{particles}} \quad \sigma_{s_v} = \sigma_{s_{v,char}} \\ where\colon \bar{\tau}_{v_{particles}} = e^{-(\kappa_v+\sigma_{s_v})\Delta s}\end{gathered} \tag{18}$$

In addition, gray particle absorption coefficients can also be implemented with the gas absorption coefficient in each wave band. By Planck averaging, the spectral particle properties, see Eq. (19), can be transformed into gray properties and implemented with the WSGGM, according to Eq. (20).

$$\begin{gathered}\kappa_{grey} = \frac{1}{I_b}\sum \Delta v I_v \, \kappa_v \\ \sigma_{s,grey} = \frac{1}{I_b}\sum \Delta v I_v \, \sigma_{s,v}\end{gathered} \tag{19}$$

$$\kappa_{WSGGM} = \kappa_{gas} + \kappa_{grey_{particles}} \tag{20}$$

In Eq. (19), the black-body and spectral intensities are determined by the particle temperature. The spectral intensity is the intensity of a spectral band, and Δv is the width of the band. This thesis employs Eqs. (19) and (20) for the coal flames (**Papers I** and **III**) to estimate the radiative contributions from the particles and gases. For the particles, it is assumed that the temperature is equal to the surrounding gas and they are evaluated in spectral bands within the IR spectra, ranging from wavenumbers 100–20000 cm^{-1}. The bandwidth is 50 cm^{-1}.

Utilizing the DOM for a cylindrical, three-dimensional enclosure to calculate the intensity, a radiative path along a discrete ordinate is in the nodal point of a computational cell that is assumed to spread in all directions in a spherical pattern. As such, the intensity is evaluated one sphere quadrant at a time. Thus, the intensity to node-point, P, from one direction in a octant of the sphere, where a ray originates from the wall boundary, gives Eq. (21) [7]:

$$I_{m,P} = \frac{\mu_m A I_A + \eta_m B I_B + \xi_m C I_c + \frac{\alpha I_\alpha}{w_m} + (\kappa I_b + \sigma_s I_{scat})V_P}{\mu_m A + \eta_m B + \xi_m C + \frac{\alpha}{w_m} + (\kappa + \sigma_s)V_P} \tag{21}$$

Equation (21) includes several variables: the directional cosines, μ_m, η_m, ξ_m, and quadrature weight, w_m; cell wall areas A, B, and C, where the radiation enters and leaves in the radial, angular, and axial directions, respectively; correction for the cylindrical curvature, α; the cell volume V at node point P; the upstream intensities I_A, I_B, and I_C, estimated through a diamond scheme [19]; and the absorption and scattering coefficients, as in Eq. (19) and Eq. (20), along with the black-body intensity and the scattered intensity, I_{scat}. I_{scat} is determined as the total of the integrated radiation from all directions. Since part of the incoming radiation is assumed to scatter isotropically in this work, I_{scat} is divided by 4π.

4. Models

The heat transfer models developed within this thesis examine the various complexities inherent to radiative heat transfer modeling, as illustrated in Figure 8. With increasing complexity, the computational effort (computational time) and resources (memory usage) increase, necessitating vital sub-model selections and assumptions in the different frameworks.

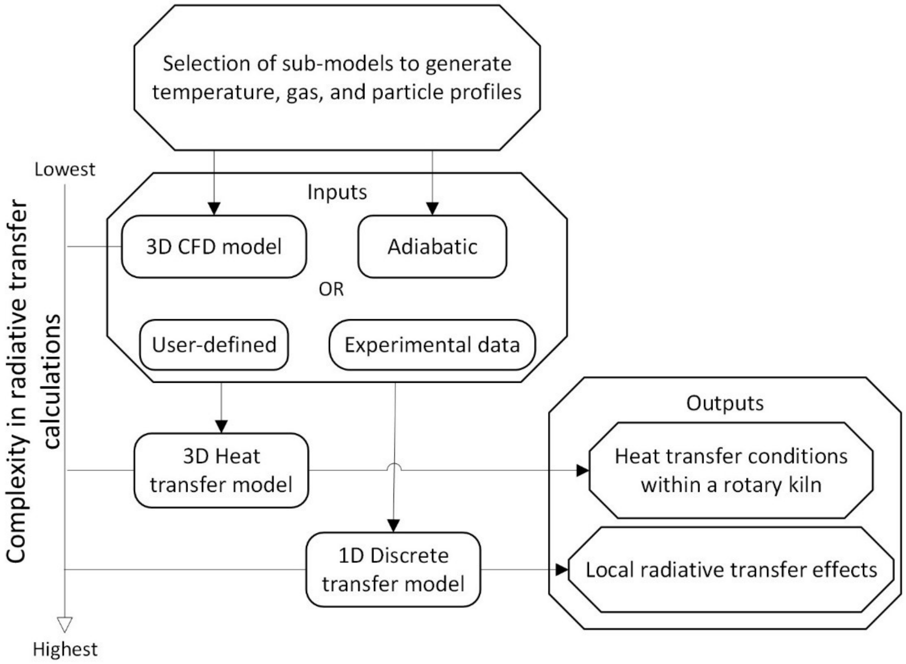

Figure 8: Flowchart of the models included in this thesis and their differences in terms of complexity for radiative transfer calculations.

In summary, this thesis employs the heat transfer model developed by Gunnarsson et al. [21], which includes detailed descriptions of the heat transfer mechanisms within kilns in a 3D framework. The heat transfer model compares various fuels, such as pulverized coal, to hydrogen gas or thermal plasmas, studying the effects on the heat transfer conditions within kilns. The complexity of the heat transfer calculations depends on the inputs to the model. These inputs can be determined through various methods: adiabatic conditions, such as those presented in **Paper I**, providing an ideal case to study heat transfer conditions within kilns during the combustion of a variety of fuels; experimental data obtained from pilot-scale test furnaces, as investigated by Gunnarsson et al. [8]; and through CFD, as presented in **Paper III**, providing inputs based on detailed modeling that includes combustion chemistry, fluid dynamics, and radiative transfer. The chosen method depends on the specific kiln conditions, the availability of experimental data, and the affordability of the computational approach.

In addition, to examine radiative transfer locally this work includes a DTM, which is geometrically limited to one dimension. The inputs used for the DTM are either user-defined inputs, representing the combustion conditions of interest, as presented in **Papers II** and **III**, or those obtained through CFD (**Paper III**). Since the model is limited to one dimension, different radiation models and modeling strategies can be evaluated, for example, by comparing the performance levels of gas models of varying complexity. Thus, the DTM used in this work also allows us to evaluate numerical errors among different gas models and to identify methods to optimize computational efficiency within more-complex geometries and modeling frameworks. The results obtained from the DTM facilitate sub-model selection for the heat transfer model and CFD codes.

As such, selecting the appropriate model for radiative transfer calculations depends on the objectives, achieved either by comparing sub-models with the DTM or conducting heat transfer analyses within kilns using the heat transfer model and CFD.

4.1 Heat transfer model

The heat transfer model used in this thesis describes the heat transfer within a full-scale rotary kiln and is described in detail elsewhere [20] [21]. The model includes: gas radiation from the hot H_2O/CO_2 gases modeled by the WSGGM [Eqs. (4) and (5)]; particle radiation from particles suspended in the flame modeled according to Mie theory [Eq. (15)] and Rayleigh theory [Eq. (16)], in combination with the WSGGM [Eq. (20)]; surface radiation from the kiln surfaces, treated as gray and diffusive; convection from the flue gas flow; and conduction through the kiln wall. In addition, the model considers heat losses from the outer wall of the kiln that occur via radiation and convection, as well as the heat generated by chemical reactions from the product material, which forms a solid bed within the kiln. Furthermore, the model accounts for the kiln's rotation, dividing the bed surface into two distinct layers: a bottom layer, and a surface layer. The bottom layer follows the rotation of the kiln wall (in the angular direction), and the surface layer moves in the opposite direction to the bottom layer. Eventually, the bottom layer is mixed into the surface layer. The bed is treated as a flat surface, determined from a specified filling degree – a furnace volume portion filled with the bed material – and is accounted for during cell discretization. The flat surface assumption has negligible effects on the radiation from/to the material or on the convective heat transfer to the material. The bed material projects an area towards the inner kiln wall surfaces comparable to a flat surface, and the heat transfer coefficients for convective transfer applied in this work depend solely on the flow size.

The heat transfer model requires several inputs, including temperature, gas, and particle profiles. The DOM is then applied, dividing the cylindrical enclosure into computational cells in three directions: axial, radial, and angular. The RTE is solved iteratively within the 3D enclosure, and the bed and wall temperatures are updated in each iteration from the calculated heat transfer contributions of radiation, convection, and conduction. The bottom layer is in contact with the kiln wall and is subjected to conductive heat transfer, which is treated in the model by applying a penetration model. The surface layer, which is exposed to gases, particles, and the kiln wall, is subjected to convective heat transfer, with coefficients obtained from the work of Gorog et al. [78], and radiative heat transfer, calculating the flux from Eq. (11) and the corresponding intensities from Eq. (21). For all the heat transfer mechanisms, the heat transfer rate is estimated from the residence time of the bed material within a computational cell, determined by the product flow rate, kiln's rotation and inclination angle. At a defined point, a computational cell in the angular direction within the bottom layer of the bed material is mixed with the surface bed layer under the assumption of perfectly mixed conditions, resulting in an average bed temperature. For a reacting bed material, several reactions have to be included and this depends on the bed material (see next section for the reactions included in this work). The outer wall heat losses due to radiation are calculated by assuming a surrounding temperature of 300 K and an outer wall temperature that is determined by the wall material properties. Losses due to convection are calculated using the outer wall convective heat transfer coefficients obtained from Barr et al. [79]. For more details of the heat transfer calculations and correlations used within the model, see [7].

The output includes the heat transferred by radiation, convection, and conduction to the kiln surfaces, the enthalpy changes in the colder secondary gas stream, and heat losses. As such, the overall heat balance, illustrated in Figure 9, is the energy over the fuel heat release transferred to the bed material boundary (via radiation, convection, and conduction), heat losses from the outer wall boundary (via radiation and convection), and the enthalpy change (between the inflowing secondary gas and outflowing flue gas).

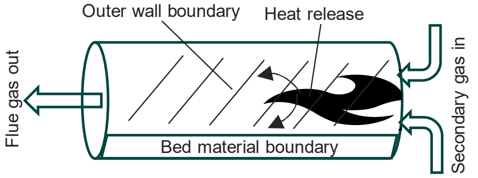

Figure 9: Overall heat balance solved by the heat transfer model.

The overall heat balance, Figure 9, is closed by iteratively specifying the flue gas temperature. Using a guessed flue gas temperature, the heat transfer model solves the total heat transfer in the kiln, and the difference between the fuel heat release and the total heat transfer, the error, is checked. The model is considered to be converged when the error for the overall heat balance is within 1%.

Modeling setup

In this thesis, two kilns are analyzed: industrial-scale kilns for iron ore production and demonstration-scale kilns for cement production. Table 1 presents the setups used to model these kilns.

Table 1: Modeling setups for the two kilns analyzed in this thesis.

Product	**Dimensions [m]**	**Bed flow** $[kg/s]$	**Bed feed temperature [°C]**	**Secondary gas flow** $[Nm^3/s]$	**Secondary gas temperature [°C]**	**Kiln rotation** $[RPM]$
Iron ore	Length: 33 Radius 2.6	~150	1000	Air: 58.85–40	Air: 1150-1200	1.6-2.0
Cement	Length: 18 Radius 0.48	~3.6	900	CO_2: 1.74	CO_2: 980	3.8

Iron ore kilns

The primary objective of the iron ore kilns included in this work is to sinter iron ore pellets through oxidizing magnetite to hematite and heat treatment, achieving temperatures of approximately 1200°–1300°C [80]. Before entering the kiln, the pellets are preheated to 1000°C by the flue gases that exit the kiln. To promote pellet oxidization during preheating, large quantities of preheated air, around 40–60 Nm^3/s at 1150°–1200°C (Table 1), are typically supplied to the kiln process during combustion, ensuring an oxygen concentration of ~16% in the kiln flue gas. The pellets are oxidized from magnetite to hematite according to Reaction (R1) [81], which is an exothermic process.

$$4\,Fe_3O_4 + O_2 \rightarrow 6\,Fe_2O_3 \quad \Delta H = -119\ kJ/mol \qquad (R1)$$

In this thesis, the heat transfer model assumes that the pellets enter the kiln, representing an industrial kiln used for iron ore production (see specifications in Table 1), with a degree of oxidation of 85%. The pellets are further oxidized within the kiln according to Reaction (R1), adding the heat of reaction as a source term, which is assumed to be evenly distributed along the kiln axis. The size and temperature of the secondary air flow mimic typical full-scale production. **Papers I** and **III** utilize the heat transfer model, providing the heat transfer conditions within iron ore kilns for conditions relevant to pulverized coal and hydrogen gas.

Cement kilns

In cement kilns, powdered raw meal is sintered by supplying sufficient heat such that the material undergoes calcination and clinkerization. Similar to iron ore kilns, the hot flue gases exiting the kiln are used to preheat the powered raw meal before it enters the kiln. The raw meal is preheated to 900°C to promote calcination, as in Reaction (R2) described by Watkinson and Brimacombe [82].

$$CaCO_3 \rightarrow CaO + CO_2 \quad \Delta H = 1700\ kJ/kg\ CaCO_3 \qquad (R2)$$

Reaction (R2) is endothermic, dissociating calcium carbonate to form calcium oxide and carbon dioxide. In the heat transfer model, the raw meal is partially calcinated within the kiln according to Reaction (R2). In addition, the model includes clinkerization – a series of complex chemical reactions needed to produce the cement-containing components (mainly alite and belite) – which occurs between the calcination and sintering temperatures, i.e., 900°C to 1450°C [83] [6]. All the heat generated or consumed by the calcination reaction (R2) or by the clinkerization reactions are determined from the enthalpies estimated using the FactSage software, and as a function of the bed material temperature.

As a low-carbon alternative heat source for modeling cement kilns, the heat transfer model applies electrically generated thermal plasmas (**Paper III**), specifically when using CO_2 as the working gas, as CO_2 from the calcination reaction is inherent to the cement process. The resulting flue gases will, thus, contain high carbon dioxide concentrations, facilitating efficient carbon capture if integrated with a CCS technology. Moreover, by excluding air as the oxidant for combustion, the process eliminates NO_x formation. In Table 1, the cement kilns represent a demonstration scale, and the CO_2 working gas is heated using 8 MW of electric power with a corresponding efficiency of 90% [83]. The secondary gas is assumed to be CO_2, maintaining the same temperature as in industrial conditions, and the flow size is scaled from typical full-scale conditions.

4.2 Model inputs

The temperature, gas, and particle profiles required by the heat transfer model depend on the heat source and the selected sub-models, such as combustion, turbulence, and radiation models, as well as the modeling strategy. The sub-model selection is vital, as it will affect the overall heat balance (see Fig. 9), i.e., the output from the heat transfer model.

Adiabatic profiles

The adiabatic flame temperature is achieved by assuming that no losses occur when the energy is released from the fuel, whereas all the energy goes into raising the temperature of the gas. Depending on the sizes of the primary and secondary air streams, an air-to-fuel ratio (AFR) can be determined, providing an estimation of the amount of excess air that will mix with the flue gases. As more air is mixed, the temperature rise in the system decreases, thereby lowering the adiabatic flame temperature. As such, the centerline of the flame can be correlated to the AFR and the adiabatic flame temperature of the applied fuel.

If the flame length, shape, and temperature distribution from the centerline are unknown, they must be assumed. In this thesis, these assumptions are illustrated in Figure 10a, which considers an axisymmetric conical flame shape with a radially linear temperature decrease from the flame centerline to the outer cone boundary. In the axial direction, plug flow is reached at the end of the flame length. As such, a local AFR is determined for each cell in the axial direction, z, within the flame, according to Eq. (22). In Eq. (22), as the flame widens into a cone and approximates the kiln radius, the AFR decreases towards plug flow conditions, and the temperature distribution along the flame centerline for each axial cell follows the adiabatic flame temperature profile of the fuel (see Fig. 10b). The gas concentration of the flame is determined from the adiabatic flame temperature.

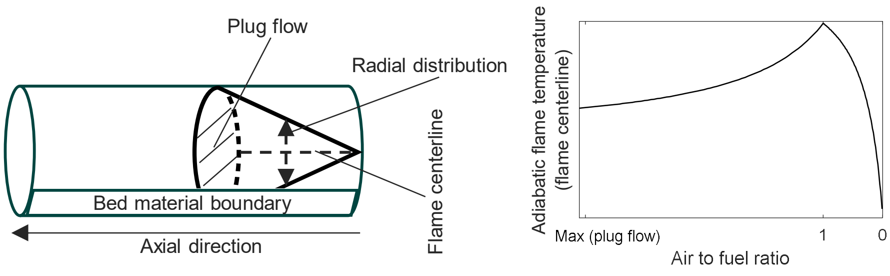

(a) (b)

Figure 10: The flame assumptions within the kiln (a), and an example of the adiabatic flame temperatures (b).

$$AFR_z = \frac{R^2_{flame,z}}{R^2_{kiln,z}} AFR_{\max\,(plug\;flow)} \tag{22}$$

The combined assumptions and adiabatic flame temperature profile map the temperature field within the kiln. Temperature fields for various fuels can then be used as an input to the heat transfer model, to calculate the isolated effects of the temperature, gas, and particle fields on the overall heat transfer conditions.

Profiles derived using experimental data

Previous work conducted by this research group, presented in Gunnarsson et al. [8], include experimental measurements performed in a 580-kW, pilot-scale test furnace that represents a stationary cylindrical furnace without bed material. The study measured the radiative intensity, temperature, gas concentration (H_2O and CO_2), and particle (char and soot) concentrations in axial ports located equidistantly along the furnace, yielding (for temperature and gas) radial data for each axial port. The gathered data were then interpolated to map the temperature and gas concentration within the furnace. For particles, the data were collected at the center position of the axial ports at fractions of the flame length. The particle data were then fitted to the radiative intensity measurements along the furnace, where it could be assumed that the particles were distributed throughout the furnace cross-section, resembling a cosine distribution with peak value in the center. In this work, the method presented previously [8] was used to implement particles in the heat transfer model, so as to study the radiation effects under adiabatic flame conditions.

Profiles derived using CFD

Alternatively, the temperature, gas, and particle profiles can be modeled by computational fluid dynamics (CFD) codes; these calculations are often used in industry to model non-reacting and reacting flows. Such codes involve solving the governing transport equations for mass, momentum, energy, and chemical species. A typical solver technique applied in commercial CFD software is the finite volume method. This method involves integrating the transport equations over many computational cells, discretization, and iteration, in order to generate the flow and temperature fields. Depending on the problem, CFD codes can include the use of several sub-models, in order to increase the complexity of the calculations to capture the studied physics. Examples of sub-models used in this thesis are: combustion models with the appropriate kinetic setups for chemical species transport for fuels, such as coal, hydrogen, and thermal plasmas with CO_2 as the working gas; turbulence modeling through applying the SST-k ω model; and transport by radiation, utilizing the DOM. Transport by radiation is included in the CFD calculations as a source term in the energy equation, determined by locally absorbed and emitted radiative energy. As described in Chapter 3, the radiative intensity, which depends on the participating particles and gases, can be calculated by the different models available in commercial CFD software packages or by implementing user-defined functions.

This work combines combustion, turbulence, and radiation sub-models in CFD modeling, which generates the flow field, with the detailed descriptions of heat transfer included in the heat transfer model that represents a rotary kiln. Thus, by constructing a CFD model that represents the same 3D full-scale rotary kiln with the same bed material as in the heat transfer model and maintaining many of the boundary conditions, the CFD-modeled profiles can be extracted to the heat transfer model to study the effect of fuel shifting on the overall heat transfer.

The approach involves interpolating the temperature, gas composition, and particle concentration node data within the kiln geometry to a mesh that is compatible with the heat transfer model. Specifically, this requires obtaining the values of the temperature, gas, and particle concentrations at all nodes in the x-, y-, and z-directions, along with the coordinates of the generated mesh. Since the values for the gas volume are of interest for extraction, the mesh must be constructed so as to exclude the bed material. Furthermore, the node data from the CFD model are considerably larger than the generated mesh. Therefore, for the interpolation, the nearest-neighbor algorithm is employed, such that a node in the generated mesh assumes the closest value that lies within the larger CFD gridded dataset. This algorithm was found to give the best results, as opposed to linear interpolation, which creates intermediate values.

In this work, the commercial software ANSYS FLUENT (2011) is used for the CFD calculations for coal-fired, hydrogen-fired, and thermal plasma-heated kilns, as presented in **Paper III**. The mesh is constructed within the MATLAB R2023b software as a cylindrical coordinates grid representing the cylindrical geometry of the kiln, which consists of nodes in the axial, angular, and radial directions. An example of the grid, where the bed material has been accounted for, is illustrated in Figure 11.

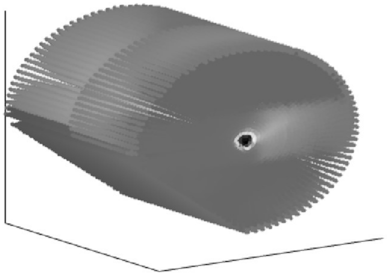

Figure 11: Cylindrical grid that is compatible with the heat transfer model.

4.3 Discrete transfer model

The DTM used in this thesis solves the radiative source term, Eq. (12), with the directional cosines gathered from Fiveland's S_{12} discrete quadrature scheme [84], in a 1D slab that consists of a gaseous domain between two infinite black plates. Defining the distance between the plates with temperature and gas profiles representative of the desired combustion conditions allows one to study the local radiative transfer effects. Here, it includes evaluating the predictive capabilities of two types of gas radiation models: the less-detailed WSGGM [intensities from Eq. (10)]; and the more-complex SNBM [intensities from Eq. (9b)], in user-defined isothermal/non-isothermal and homogeneous/non-homogeneous 1D domains (for details, see **Paper II**). The non-isothermal/non-homogeneous domains are defined by assuming that the temperature and/or gas profile varies according to a cosine profile that ranges from the temperature/gas concentration at the plate walls to a peak value in the domain center, according to Eq. (23). As such, Eq. (23) is a function of the plate and peak temperatures/gas concentrations, the plate distance, S_m, and the coordinates in a radiative path between the plates, s.

$$\begin{gathered} T/Y_{profile} = Constant_1 - Constant_2 cos(2\pi s/S_m) \\ where: \\ Constant_1 = \frac{T/Y_{plates} + T/Y_{peak}}{2} \;\&\; Constant_2 = \frac{T/Y_{peak} - T/Y_{plates}}{2} \end{gathered} \tag{23}$$

The accuracy is assessed by the average deviation, ξ, from the SNBM in predicting the radiative source term (for non-isothermal and/or non-homogeneous domains) or total emissivity (for isothermal and homogeneous domains) over the pathlength within the domain, according to Eq. (24):

$$\begin{gathered} \xi = \int_0^S |\varepsilon_{WSGG} - \varepsilon_{SNBM}| / \int_0^S |\varepsilon_{SNBM}| \\ \xi = \int_0^{S_m} |\nabla q_{WSGG} - \nabla q_{SNBM}| / \int_0^{S_m} |\nabla q_{SNBM}| \end{gathered} \tag{24}$$

Furthermore, in **Paper III**, the DTM is used to investigate local radiative transfer effects by calculating the source term in one cross-section of the coal/hydrogen-fired and plasma-heated kilns. Here, the temperature and gas profiles are defined from CFD simulations, and the gas emissions defined by the WSGGM parameters presented in **Paper II** are compared for gray/non-gray formulations [Eqs. (10a) and (10b)] to the SNBM [Eq. 9b)].

Radiative source term cases

With the DTM, two radiative source term cases are included for analysis, and are presented in the results. These cases examine the local radiative transfer effects under conditions relevant to coal and hydrogen combustion. Several WSGGMs are employed and compared to the SNBM: the new WSGGM presented in **Paper II**; the WSGGM of Smith and Shen [24], which is commonly used in CFD codes for conventional combustion conditions; the WSGGM of

Johannsson [23], which is applied in **Paper I** to model the gas emissions from coal flames; and the WSGGM of Bordbar et al. [26], which is also applied in **Paper I** to model the gas emissions from hydrogen flames. The Smith, Johansson, and Bordbar WSGGMs are all limited with respect to temperature, to <2400/2500 K. Therefore, two temperature profiles are applied for the analysis: Eq. (25a) relevant to coal combustion, and Eq. (25b) relevant to hydrogen combustion. The profiles are assumed to follow a cosine function, as in Eq. (23), ranging from preheated air temperatures for iron ore kilns, 1473 K (see Table 1) to the calculated peak adiabatic temperatures of the coal and hydrogen flames in **Paper I**.

$$T = 1650 - 450\ cos(2\pi s/S_m) \tag{25a}$$

$$T = 2200 - 1000\ cos(2\pi s/S_m) \tag{25b}$$

For Eq. (25a), the gas concentration in the domain is constant, with an H_2O to CO_2 molar ratio of unity, such that it is within the Smith WSGGM boundaries. For Eq. (25b), it is 100% H_2O. The plate walls are set to maintain a temperature of 500 K, and the plate distance, S_m, is 5 m, representing the diameter of the iron ore kiln (Table 1). The WSGGM deviation from the SNBM, ξ, is determined according to Eq. (24), where a deviation from the SNBM of around 20% is, according to a previous study [23], considered to be acceptable.

5. Results

The result of this thesis cover two types of models: 1D problems for predicting the radiative source term in a slab (see Section 4.3), and 3D problems for predicting the heat transfer conditions within iron ore kilns using the heat transfer model (see Section 4.1).

5.1 Radiative source term calculations in a one-dimensional slab

The results from the source term calculations are presented and illustrated in Figure 12, a and b, and the deviations from the SNBM are listed in Table 2.

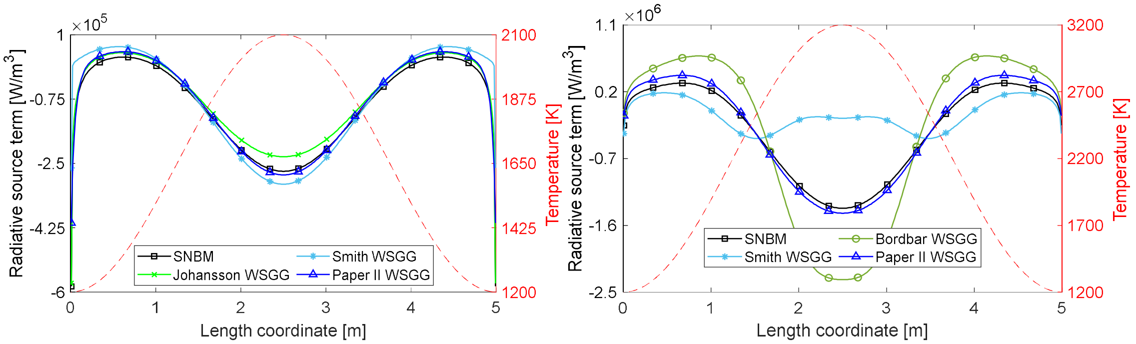

(a) *(b)*

Figure 12: Radiative source term calculations for a domain relevant to conventional combustion (a), and for pure hydrogen combustion (b). The red dashed line represents the applied temperature profile.

Table 2: Case specification and the deviation relative to the SNBM, as in Eq. (24), for the tested WSGGMs.

Case	***Temperature profile***	***Gas concentration***	***ξ: Paper II***	***ξ: Smith***	***ξ: Bordbar***	***ξ: Johansson***
Fig. 12a	Eq. (25a)	$\frac{Y_{H2O}}{Y_{CO2}} = 1$	11%	28%	-	18%
Fig. 12b	Eq. (25b)	$Y_{H2O} = 100\%$	15%	77%	88%	-

Figure 12a shows the performances of the mentioned WSGGMs for temperatures that are relevant to coal combustion. In Figure 12a, a gradient of deviation relative to the SNBM is observed for the Smith and Johansson WSGGM, specifically in the hot domain center. Among the WSGGMs tested, the WSGGM presented in **Paper II** exhibits the highest accuracy (see Table 2) compared to the SNBM, and its performance is considered acceptable.

Figure 12b shows the source term when the temperatures exceed the validity range of conventional WSGGMs, such as those relevant for hydrogen combustion. For those models, more-prominent gradients of deviations from the SNBM are observed throughout the domain compared to coal combustion conditions. However, the WSGGM in **Paper II**, again, performs at a satisfactory level, while the WSGGMs of Bordbar and Smith predict the source term with deviations that exceed the acceptable 20% range relative to the SNBM.

The observed source term trends in Figure 12, a and b are similar. Close to the walls, the source term is negative due to the temperature gradient between the cold walls (500 K) and hot gas (~1200 K), resulting in gas emission. The gas temperature increases towards the peak in the domain center, where the gases emit radiation. At distances of around 0.5 m (Fig. 12a) and 0.25–1.25 m (Fig. 12b) from the walls, the source term is positive, as the gas mixture absorbs radiation from the hotter gases in the domain center. The source term is positive in a broader range for Figure 12b compared to Figure 12a, due to the higher gas temperatures in the peak.

In summary, the results highlight the need for accurate sub-model selection for predicting gas radiation, specifically during combustion modeling that involves pure hydrogen as the fuel. The performance of the WSGGM from **Paper II** shows its suitability for both coal and hydrogen combustion conditions.

5.2 Three-dimensional heat transfer calculations within kilns

This section compares the modeled heat transfer conditions within a rotary kiln for coal and hydrogen flames under adiabatic conditions (presented in **Paper I**) to the CFD-modeled coal and hydrogen flames (presented in **Paper III**), including the new gas radiation model presented in **Paper II**. The temperature profiles of the flames are illustrated in Figure 13.

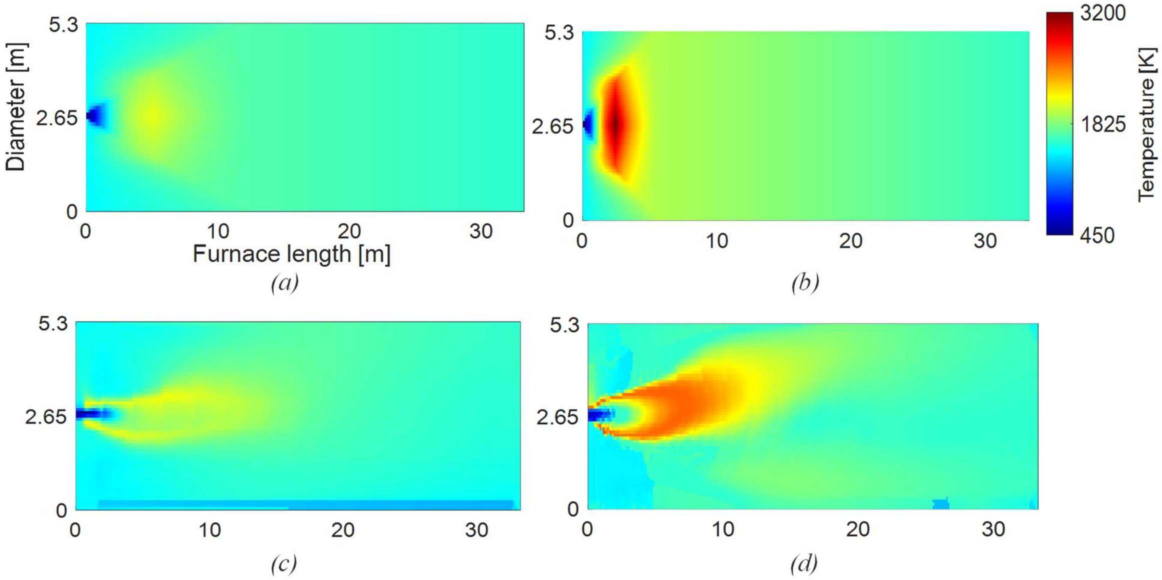

Figure 13: Temperature contours of the coal flame (a) and hydrogen flame (b) under adiabatic conditions (flue gas temperatures of 1596 K and 1617 K, respectively), and as a result of CFD-modeled conditions for the coal flame (c) and hydrogen flame (d) (with flue gas temperatures of 1578 K for both flames).

The comparison includes the calculated heat transfer from fuel heat release (via radiation, convection, and conduction) to the product bed material and the flue gases (see Table 3). Since the fuel heat release differs between the cases, the heat transfer rates to the bed and flue gases are presented relative to the fuel heat release. In addition, to account for differences in the secondary gas flows and temperatures (40 Nm^3/s and 1473 K in **Paper I**; and 58.85 Nm^3/s and 1423 K in **Paper III**), the heat transfer to the flue gas is normalized by the secondary gas flow rate. Furthermore, the comparison includes the temperature profiles of the product and kiln wall, as determined from the resulting heat transfer calculations (Fig. 14).

*Table 3: Heat transfer conditions for the adiabatic coal and hydrogen flames in **Paper I**, and the CFD-based coal and hydrogen flames in **Paper III**, applying the WSGGM from **Paper II**.*

Case	**Coal Adiabatic**	**Coal CFD**	**H_2 Adiabatic**	**H_2 CFD**
Fuel heat release (MW)	35	37	35	41
Heat transfer to bed (relative to fuel heat release)				
Radiation	57%	49%	53%	26%
Convection	9%	5%	14%	8%
Conduction	3%	4%	3%	2%
Sum	68%	58%	70%	37%
Heat to flue gas	29%	47%	28%	53%
Normalized heat to flue gas (MW/$\frac{Nm^3}{s}$ 2nd gas)	0.26	0.29	0.24	0.36

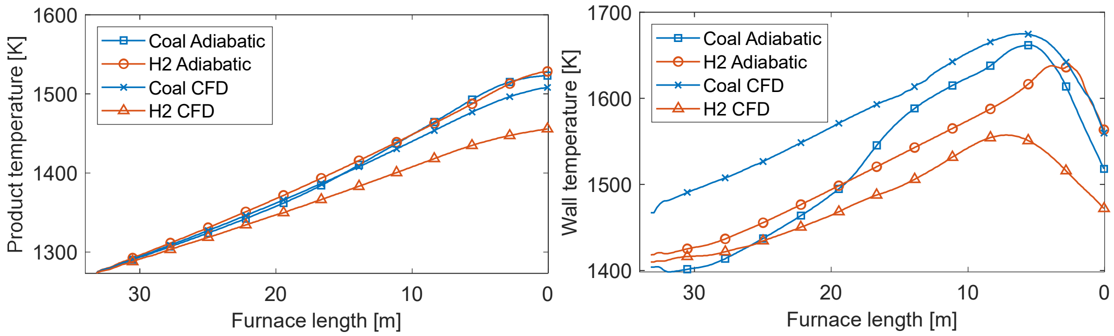

(a) *(b)*

Figure 14: Temperature profiles of the product (a) and kiln wall (b).

Adiabatic- and CFD-based coal flames

Under adiabatic conditions, the coal flame predicts a total heat transfer fraction to the bed material that is ~17% higher than that of the CFD-based coal flame (see Table 3 and Fig. 14a). The majority of the heat transfer difference arises from radiation (fraction is ~16% higher in the adiabatic flame) and convection (fraction is ~80% higher in the adiabatic flame). The overall heat balance is considered to be closed, showing only 0.1% and 8% differences in total heat transfer rate and heat release between the adiabatic and CFD-coal flames, respectively.

The adiabatic flame results in higher gas temperatures compared to the CFD flame (see Fig. 13), leading to increased radiative heat transfer from the suspended particles and gases. Furthermore, due to the conical shape of the flame, the temperature of the gas layers adjacent to the kiln surfaces is higher, promoting more-efficient convective heat transfer. As a result, the overall heat transfer under CFD-modeled conditions is not as efficient as under adiabatic conditions, and more heat exits with the flue gases (~62% more heat transfer fraction to the flue gas under CFD than under adiabatic conditions, and higher heat to flue gas per unit of secondary gas flow under CFD conditions). However, the flue gas temperatures are similar between CFD and adiabatic (see Fig. 13). Moreover, differences in wall temperature profiles, as illustrated in Figure 14b, indicate that the heat transfer rate to the kiln wall is higher in the CFD case. The reason for this is the different particle profiles; in the CFD case, particles travel farther downstream in the furnace, and along with the surrounding gases, they participate in radiation over a greater distance than in the adiabatic case.

Adiabatic- and CFD-based hydrogen flames

In the hydrogen cases, significant differences are observed between the adiabatic- and CFD-modeled conditions (see Table 3 and Fig. 14). The total fraction of heat transferred to the bed material is ~89% higher in the adiabatic case, with the radiative contribution (fraction) being ~103% higher and the convection contribution being 75% higher than the CFD case. Consequently, the heat transfer fraction to the flue gases and the normalized heat to flue gas per unit of secondary gas flow are 89% and 50% higher in the CFD case than in the adiabatic case, respectively. Again, the overall heat balance is considered closed for the two cases, showing 0.1% and 6% differences in total heat transfer rate and heat release between the adiabatic and CFD-hydrogen flames, respectively. The higher peak flame temperatures in the adiabatic case result in increased radiative heat transfer, primarily due to H_2O gas emissions. Here, it should be noted that the adiabatic case (**Paper I**) applies the gas radiation model (WSGGM) of Bordbar [26], which is limited to temperatures below 2400 K. The associated errors when exceeding the model's limit are described in Section 5.1.

CFD-based flames: coal vs hydrogen

As shown in Figure 13, the CFD-based hydrogen flame achieves higher peak gas temperatures than the coal flame, but has lower heat transfer rates to the bed material (see Table 3). The reason for this is the lack of radiating particles in the hydrogen flame. Consequently, the lower heat transfer rates to the kiln surfaces result in the lowest product and wall temperatures among the studied cases, as illustrated in Figure 14.

In summary, using CFD increases the precision of the calculations because the framework allows the integration of selected sub-models for combustion, turbulence, and radiation into the defined transport equations. Furthermore, applying the updated WSGGM (**Paper II**) increases the precision of describing gas emissions, specifically for temperatures above 2400

K. The impact of the fuel shift is observed locally in terms of the heat transfer to the kiln wall, with the variations depending on the complexity between cases. The heat transfer during hydrogen firing is not as efficient as during coal firing. To increase efficiency, co-firing hydrogen with coal may be considered, as adding particles may effectively enhance the radiative heat transfer rate within the furnace. However, results from **Paper I** indicate that adding particles to a hydrogen flame will, once again, exert a local effect on the overall heat transfer rate, specifically close to the burner region. Therefore, such calculations will require greater precision, achieved via careful sub-model selection.

6. Conclusions

This work develops models to increase understanding of thermal radiation and its effects on the overall heat transfer within rotary kilns when substituting fossil-based fuels with electrification through hydrogen gas or thermal plasmas.

This thesis includes: a heat transfer modeling study of coal and hydrogen-fired kilns under adiabatic flame temperature conditions **(Paper I)**; the generation of updated parameters for a weighted-sum-of-gray-gases model to extend its applicability to H_2O/CO_2 gas mixtures at up to 5000 K **(Paper II)**; the evaluation of WSGGMs in CFD codes (**Paper III**); and the use of a 1D discrete transfer model to study the local radiative effects during fuel shifting (**Paper III**).

Radiative source term calculations show that for conditions relevant to hydrogen combustion, the WSGGM derived for higher temperatures presented in **Paper II** outperforms the other WSGGMs tested. This highlights the importance of selecting appropriate gas radiation models, especially for predicting radiative heat transfer in hydrogen flames.

Using CFD modeling with selected sub-models for combustion, turbulence, and radiation increases the complexity and precision of the calculations compared to adiabatic modeling. The updated WSGGM (**Paper II**) increases the precision of radiative predictions through gas emissions, which dominates heat transfer in the modeled hydrogen flames, as compared to the current standard model. The results show that under adiabatic conditions, the hydrogen flame predicts heat transfer rates at levels comparable to those for the coal flame. However, using CFD-based conditions, the overall heat transfer is lower for the hydrogen flame than for the coal flame. The reason for this is the lower peak flame temperatures (compared to adiabatic) and the lack of particles, which reduces the radiative heat transfer rates. As a result, the majority of the heat transferred from fuel heat release exits with the flue gases, indicating lower heat transfer efficiency compared to coal firing.

In conclusion, the transition from coal firing to hydrogen firing in kilns affects the overall and local heat transfer rates, as observed in the kiln temperature profiles. The results show the importance of sub-model selection for describing the flame conditions (adiabatic flame temperature conditions are not optimal) and for accurately estimating the gas emissions (through appropriate gas model selection) in kilns during either coal or hydrogen firing. Although hydrogen firing effectively reduces the levels of carbon dioxide emissions and particulate formation, its heat transfer efficiency in rotary kilns is lower than that of coal, necessitating co-firing or alternative kiln designs.

7. Future work

The findings presented in this thesis indicate several directions for future research aimed at increasing our understanding of the heat transfer conditions in rotary kilns. Future studies should:

- Study the interactions of particles suspended in a hydrogen flame and their effects on the overall and local heat transfer rates to the kiln surfaces.
- Perform model validation by comparing the updated WSGGM parameters against radiative intensity measurements made under conditions relevant to hydrogen flames or thermal plasmas, thereby assessing the accuracy levels of the model parameters in radiative transfer.
- Evaluate the effects of dissociation on radiation by generating WSGGM parameters that include, for instance, the radiative contribution from the dissociation of CO_2 to CO molecules and other radicals.
- Examine methods that combine radiation modeling with optical measurement instruments to study combustion processes. It will be important to understand which optical measurements should be made during hydrogen combustion or thermal plasma heating, particularly those in the different emissions spectra, such as in the IR and visible spectra. This will facilitate the development of optical measurement techniques and increase the precision levels of our models.

Nomenclature

I	radiative intensity
$\hat{s}$	unit vector in a given direction
s	the coordinates in a radiative path
w	quadrature weight in a direction m
N	total number of discrete directions
MR	gaseous molar ratio of H_2O to CO_2
a_j	weight of gray gas j
S	pathlength
P	total pressure/node-point
Y	gaseous molar fraction of species
T	temperature
K	parameter for WSGGM
C	parameter for WSGGM
k_k	mean line-intensity to typical line-spacing within a narrow band
d_k	inverse of mean line spacing
Δs	length of a computational cell
q_r	radiative flux
∇q	radiative source term
S_m	distance between plates
S_{char}	characteristic domain length between plates
f	forward scattering factor
Q_{abs}	absorption efficiency
Q_{sca}	scattering efficiency
A_{proj}	projected particle surface area
f_f	particle volume fraction
N	number density
k_λ	absorptive index

m_λ	complex index of refraction
n_λ	refractive index
Δv	bandwidth
V	volume
R	kiln radius
A	cell surface area in radial direction
B	cell surface area in angular direction
C	cell surface area in axial direction

Greek symbols

κ	absorption coefficient
σ_s	scattering coefficient
Φ	scattering phase function/azimuthal angle
Ω	solid angle for in-scattering/direction vector of radiative intensity
Θ	polar angle
μ, η, ξ	direction cosines in x, y, z directions
ζ	any direction cosine
ε	emissivity
τ	transmissivity
γ	mean line half-width
λ	wavelength
α	geometrical coefficient
ξ	deviation from the SNBM

Subscript

m	discrete direction
v	wavenumber/spectral property
b	black-body
j	gas j in the weighted sum of gray gases model
I	polynomial degree

i	factor *i* of polynomial degree *I* / cloud of particles
k	band in the statistical narrow band model
n	cell number

Superscripts

$\bar{\ }$	averaged property
+	leaving
-	arriving

Chemical compounds

Fe_3O_4	magnetite
Fe_2O_3	hematite
$CaCO_3$	calcium carbonate
CaO	calcium oxide

References

[1] B.-J.R. Mungyeko Bisulandu, F. Huchet, Rotary kiln process: An overview of physical mechanisms, models and applications, Appl. Therm. Eng. 221 (2023) 119637. https://doi.org/10.1016/j.applthermaleng.2022.119637.

[2] K.E. Peray, J.J. Waddell, The rotary cement kiln, Edward Arnold New York, NY, USA, 1986.

[3] Jarod Ryan, CFD Modelling of Heat Transfer and Calcination in Rotary Lime Kilns, University of Toronto, 2024.

[4] C.Y.C. Jonsson, J. Stjernberg, H. Wiinikka, B. Lindblom, D. Boström, M. Öhman, Deposit formation in a grate-kiln plant for iron-ore pellet production. Part 1: Characterization of process gas particles, Energy and Fuels 27 (2013) 6159–6170. https://doi.org/10.1021/EF400973W.

[5] E. Mastorakos, A. Massias, C.D. Tsakiroglou, D.A. Goussis, V.N. Burganos, A.C. Payatakes, CFD predictions for cement kilns including flame modelling, heat transfer and clinker chemistry, Appl. Math. Model. 23 (1999) 55–76. https://doi.org/10.1016/S0307-904X(98)10053-7.

[6] B. Wilhelmsson, C. Kollberg, J. Larsson, J. Eriksson, M. Eriksson, CemZero - A feasibility study evaluating ways to reach sustainable cement production via the use of electricity, 2018.

[7] A. Gunnarsson, Radiative heat transfer in suspension-fired systems, Chalmers University of Technology, 2019.

[8] A. Gunnarsson, D. Bäckström, R. Johansson, C. Fredriksson, K. Andersson, Radiative Heat Transfer Conditions in a Rotary Kiln Test Furnace Using Coal, Biomass, and Cofiring Burners, Energy and Fuels 31 (2017) 7482–7492. https://doi.org/10.1021/ACS.ENERGYFUELS.7B00083.

[9] D. Bäckström, R. Johansson, K. Andersson, H. Wiinikka, C. Fredriksson, On the use of alternative fuels in rotary kiln burners — An experimental and modelling study of the effect on the radiative heat transfer conditions, Fuel Process. Technol. 138 (2015) 210–220. https://doi.org/10.1016/J.FUPROC.2015.05.021.

[10] A. Johansson, J. Fernberg, A. Sepman, S. Colin, J. Wennebro, F. Normann, H. Wiinikka, Cofiring of hydrogen and pulverized coal in rotary kilns using one integrated burner, Int. J. Hydrogen Energy 90 (2024) 342–352. https://doi.org/10.1016/j.ijhydene.2024.09.327.

[11] E. Fooladgar, A. Sepman, Y. Ögren, A. Johansson, M. Gullberg, H. Wiinikka, Low-NOx thermal plasma torches: A renewable heat source for the electrified process industry, Fuel 378 (2024) 132959. https://doi.org/10.1016/j.fuel.2024.132959.

[12] J. Hercog, R. Lewtak, B. Glot, P. Jóźwiak, G. Nehring, V.D. Tavares, A.M. Nunes, D. Gaspar, Pilot testing and numerical simulations of the multifuel burner for the cement kiln, Fuel 342 (2023) 127801. https://doi.org/10.1016/j.fuel.2023.127801.

[13] Y. Wang, C.H. Sohn, J.Y. Kim, Effects of hydrogen blending on combustion and pollutant emission of propane/air in a model furnace with a rotary kiln burner, Therm.

Sci. Eng. Prog. 47 (2024) 102330. https://doi.org/10.1016/J.TSEP.2023.102330.

[14] P. Barr, Heat transfer processes in rotary kilns, University of British Columbia, 1986.

[15] K.S. Mujumdar, V. V. Ranade, Simulation of rotary cement kilns using a one-dimensional model, Chem. Eng. Res. Des. 84 (2006) 165–177. https://doi.org/10.1205/cherd.04193.

[16] X. hui Fan, J. Li, X. ling Chen, Y. Wang, M. Gan, Temperature Field Simulation Model for Rotary Kiln of Iron Ore Oxidized Pellet, J. Iron Steel Res. Int. 20 (2013) 16–19. https://doi.org/10.1016/S1006-706X(13)60076-X.

[17] J.P. Gorog, T.N. Adams, J.K. Brimacombe, Heat transfer from flames in a rotary kiln, Metall. Trans. B 14 (1983) 411–424. https://doi.org/10.1007/BF02654360.

[18] J.P. Gorog, J.K. Brimacombe, T.N. Adams, Radiative heat transfer in rotary kilns, Metall. Trans. B 12 (1981) 55–70. https://doi.org/10.1007/BF02674758.

[19] M.F. Modest, Radiative Heat Transfer, 3rd edition, Elsevier, 2013.

[20] A. Gunnarsson, K. Andersson, B.R. Adams, C. Fredriksson, Discrete-ordinates modelling of the radiative heat transfer in a pilot-scale rotary kiln, Energies 13 (2020). https://doi.org/10.3390/en13092192.

[21] A. Gunnarsson, K. Andersson, B.R. Adams, C. Fredriksson, Full-scale 3D-modelling of the radiative heat transfer in rotary kilns with a present bed material, Int. J. Heat Mass Transf. 147 (2020). https://doi.org/10.1016/j.ijheatmasstransfer.2019.118924.

[22] R. Johansson, K. Andersson, B. Leckner, H. Thunman, Models for gaseous radiative heat transfer applied to oxy-fuel conditions in boilers, Int. J. Heat Mass Transf. 53 (2010) 220–230. https://doi.org/10.1016/J.IJHEATMASSTRANSFER.2009.09.039.

[23] R. Johansson, B. Leckner, K. Andersson, F. Johnsson, Account for variations in the H2O to CO2 molar ratio when modelling gaseous radiative heat transfer with the weighted-sum-of-grey-gases model, Combust. Flame 158 (2011) 893–901. https://doi.org/10.1016/J.COMBUSTFLAME.2011.02.001.

[24] T.F. Smith, Z.F. Shen, Evaluation of Coefficients for the Weighted Sum of Gray Gases Model., Am. Soc. Mech. Eng. 104 (1981).

[25] M.H. Bordbar, G. Wecel, T. Hyppänen, A line by line based weighted sum of gray gases model for inhomogeneous CO2–H2O mixture in oxy-fired combustion, Combust. Flame 161 (2014) 2435–2445. https://doi.org/10.1016/J.COMBUSTFLAME.2014.03.013.

[26] H. Bordbar, G.C. Fraga, S. Hostikka, An extended weighted-sum-of-gray-gases model to account for all CO2 - H2O molar fraction ratios in thermal radiation, Int. Commun. Heat Mass Transf. 110 (2020) 104400. https://doi.org/10.1016/J.ICHEATMASSTRANSFER.2019.104400.

[27] T. Kangwanpongpan, F.H.R. França, R. Corrêa Da Silva, P.S. Schneider, H.J. Krautz, New correlations for the weighted-sum-of-gray-gases model in oxy-fuel conditions based on HITEMP 2010 database, Int. J. Heat Mass Transf. 55 (2012) 7419–7433. https://doi.org/10.1016/J.IJHEATMASSTRANSFER.2012.07.032.

[28] J. Guo, X. Li, X. Huang, Z. Liu, C. Zheng, A full spectrum k-distribution based

weighted-sum-of-gray-gases model for oxy-fuel combustion, Int. J. Heat Mass Transf. 90 (2015) 218–226. https://doi.org/10.1016/J.IJHEATMASSTRANSFER.2015.06.052.

[29] Z. Yang, A. Gopan, Improved global model for predicting gas radiative properties over a wide range of conditions, Therm. Sci. Eng. Prog. 22 (2021) 100856. https://doi.org/10.1016/J.TSEP.2021.100856.

[30] L.J. Dorigon, G. Duciak, R. Brittes, F. Cassol, M. Galarça, F.H.R. França, WSGG correlations based on HITEMP2010 for computation of thermal radiation in non-isothermal, non-homogeneous H2O/CO2 mixtures, Int. J. Heat Mass Transf. 64 (2013) 863–873. https://doi.org/10.1016/J.IJHEATMASSTRANSFER.2013.05.010.

[31] F.R. Coelho, F.H.R. França, WSGG correlations based on HITEMP2010 for gas mixtures of H2O and CO2 in high total pressure conditions, Int. J. Heat Mass Transf. 127 (2018) 105–114. https://doi.org/10.1016/J.IJHEATMASSTRANSFER.2018.07.075.

[32] X. Cai, S. Shan, Q. Zhang, J. Zhao, Z. Zhou, New WSGG model for gas mixtures of H2O, CO2, and CO in typical coal gasifier conditions, Fuel 311 (2022) 122541. https://doi.org/10.1016/J.FUEL.2021.122541.

[33] H.C. Hottel, A.F. Sarofim, Raditive Transfer, McGraw-Hill, New York, 1967.

[34] D.K. Edwards, W.A. Menard, Comparison of Models for Correlation of Total Band Absorption, Appl. Opt. 3 (1964) 621–625. https://doi.org/10.1364/AO.3.000621.

[35] A.T. Modak, Exponential Wide Band Parameters for the Pure Rotational Band of Water Vapor, J. Quant. Spectrosc. Radiat. Transf. 21 (1979) 131–142.

[36] N. Lallemant and R. Weber, Radiative property models for computing non-sooty natural gas flames. Part 1: Report on radiation modelling. IFRF Doc No G 08/y/2, Ijmuiden, 1993.

[37] B. Leckner, Spectral and total emissivity of water vapor and carbon dioxide, Combust. Flame 19 (1972) 33–48. https://doi.org/10.1016/S0010-2180(72)80084-1.

[38] R. Johansson, B. Leckner, K. Andersson, F. Johnsson, Influence of particle and gas radiation in oxy-fuel combustion, Int. J. Heat Mass Transf. 65 (2013) 143–152. https://doi.org/10.1016/j.ijheatmasstransfer.2013.05.073.

[39] L.S. Rothman, C.P. Rinsland, A. Goldman, S.T. Massie, D.P. Edwards, J.M. Flaud, A. Perrin, C. Camy-Peyret, V. Dana, J.Y. Mandin, J. Schroeder, A. McCann, R.R. Gamache, R.B. Wattson, K. Yoshino, K. V. Chance, K.W. Jucks, L.R. Brown, V. Nemtchinov, P. Varanasi, THE HITRAN MOLECULAR SPECTROSCOPIC DATABASE AND HAWKS (HITRAN ATMOSPHERIC WORKSTATION): 1996 EDITION, J. Quant. Spectrosc. Radiat. Transf. 60 (1998) 665–710. https://doi.org/10.1016/S0022-4073(98)00078-8.

[40] L.S. Rothman, D. Jacquemart, A. Barbe, D.C. Benner, M. Birk, L.R. Brown, M.R. Carleer, C. Chackerian, K. Chance, L.H. Coudert, V. Dana, V.M. Devi, J.M. Flaud, R.R. Gamache, A. Goldman, J.M. Hartmann, K.W. Jucks, A.G. Maki, J.Y. Mandin, S.T. Massie, J. Orphal, A. Perrin, C.P. Rinsland, M.A.H. Smith, J. Tennyson, R.N. Tolchenov, R.A. Toth, J. Vander Auwera, P. Varanasi, G. Wagner, The HITRAN 2004 molecular spectroscopic database, J. Quant. Spectrosc. Radiat. Transf. 96 (2005) 139–

204. https://doi.org/10.1016/J.JQSRT.2004.10.008.

[41] L.S. Rothman, I.E. Gordon, A. Barbe, D.C. Benner, P.F. Bernath, M. Birk, V. Boudon, L.R. Brown, A. Campargue, J.P. Champion, K. Chance, L.H. Coudert, V. Dana, V.M. Devi, S. Fally, J.M. Flaud, R.R. Gamache, A. Goldman, D. Jacquemart, I. Kleiner, N. Lacome, W.J. Lafferty, J.Y. Mandin, S.T. Massie, S.N. Mikhailenko, C.E. Miller, N. Moazzen-Ahmadi, O. V. Naumenko, A. V. Nikitin, J. Orphal, V.I. Perevalov, A. Perrin, A. Predoi-Cross, C.P. Rinsland, M. Rotger, M. Šimečková, M.A.H. Smith, K. Sung, S.A. Tashkun, J. Tennyson, R.A. Toth, A.C. Vandaele, J. Vander Auwera, The HITRAN 2008 molecular spectroscopic database, J. Quant. Spectrosc. Radiat. Transf. 110 (2009) 533–572. https://doi.org/10.1016/J.JQSRT.2009.02.013.

[42] L.S. Rothman, I.E. Gordon, Y. Babikov, A. Barbe, D. Chris Benner, P.F. Bernath, M. Birk, L. Bizzocchi, V. Boudon, L.R. Brown, A. Campargue, K. Chance, E.A. Cohen, L.H. Coudert, V.M. Devi, B.J. Drouin, A. Fayt, J.M. Flaud, R.R. Gamache, J.J. Harrison, J.M. Hartmann, C. Hill, J.T. Hodges, D. Jacquemart, A. Jolly, J. Lamouroux, R.J. Le Roy, G. Li, D.A. Long, O.M. Lyulin, C.J. Mackie, S.T. Massie, S. Mikhailenko, H.S.P. Müller, O. V. Naumenko, A. V. Nikitin, J. Orphal, V. Perevalov, A. Perrin, E.R. Polovtseva, C. Richard, M.A.H. Smith, E. Starikova, K. Sung, S. Tashkun, J. Tennyson, G.C. Toon, V.G. Tyuterev, G. Wagner, The HITRAN2012 molecular spectroscopic database, J. Quant. Spectrosc. Radiat. Transf. 130 (2013) 4–50. https://doi.org/10.1016/J.JQSRT.2013.07.002.

[43] L.S. Rothman, R.B. Wattson, R. Gamache, J.W. Schroeder, A. McCann, HITRAN HAWKS and HITEMP: high-temperature molecular database, in: J.C. Dainty (Ed.), Atmos. Propag. Remote Sens. IV, SPIE, 1995: pp. 105–111. https://doi.org/10.1117/12.211919.

[44] L.S. Rothman, I.E. Gordon, R.J. Barber, H. Dothe, R.R. Gamache, A. Goldman, V.I. Perevalov, S.A. Tashkun, J. Tennyson, HITEMP, the high-temperature molecular spectroscopic database, J. Quant. Spectrosc. Radiat. Transf. 111 (2010) 2139–2150. https://doi.org/10.1016/J.JQSRT.2010.05.001.

[45] A. Soufiani, J. Taine, High temperature gas radiative property parameters of statistical narrow-band model for H2O, CO2 and CO, and correlated-K model for H2O and CO2, Int. J. Heat Mass Transf. 40 (1997) 987–991. https://doi.org/10.1016/0017-9310(96)00129-9.

[46] P. Rivière, S. Langlois, A. Soufiani, J. Taine, An approximate data base of H2O infrared lines for high temperature applications at low resolution. Statistical narrow-band model parameters, J. Quant. Spectrosc. Radiat. Transf. 53 (1995) 221–234. https://doi.org/10.1016/0022-4073(95)90009-8.

[47] D. Scutaru, L. Rosenmann, J. Taine, Approximate intensities of CO2 hot bands at 2.7, 4.3, and 12µm for high temperature and medium resolution applications, J. Quant. Spectrosc. Radiat. Transf. 52 (1994) 765–781. https://doi.org/10.1016/0022-4073(94)90042-6.

[48] J.-M. Flaud, C. Camy-Peyret, R. Toth, Water Vapour Line Parameters from Microwave to Medium Infrared An Atlas of H2160, H2170 and H2180 Line Positions and Intensities between 0 and 4350 cm-1, 1st ed., Elsevier, 1981. https://doi.org/10.1016/C2013-0-03414-7.

[49] P. Rivière, A. Soufiani, Updated band model parameters for H2O, CO2, CH4 and CO

radiation at high temperature, Int. J. Heat Mass Transf. 55 (2012) 3349–3358. https://doi.org/10.1016/J.IJHEATMASSTRANSFER.2012.03.019.

[50] H. Chu, F. Liu, H. Zhou, Calculations of gas thermal radiation transfer in one-dimensional planar enclosure using LBL and SNB models, Int. J. Heat Mass Transf. 54 (2011) 4736–4745. https://doi.org/10.1016/J.IJHEATMASSTRANSFER.2011.06.002.

[51] V. Becher, S. Clausen, A. Fateev, H. Spliethoff, Validation of spectral gas radiation models under oxyfuel conditions. Part A: Gas cell experiments, Int. J. Greenh. Gas Control 5 (2011) S76–S99. https://doi.org/10.1016/J.IJGGC.2011.05.005.

[52] D.K. Edwards, Molecular Gas Band Radiation, Adv. Heat Transf. 12 (1976) 115–193. https://doi.org/10.1016/S0065-2717(08)70163-1.

[53] A.T. Modak, Exponential wide band parameters for the pure rotational band of water vapor, J. Quant. Spectrosc. Radiat. Transf. 21 (1979) 131–142. https://doi.org/10.1016/0022-4073(79)90024-4.

[54] J. Ströhle, P.J. Coelho, On the application of the exponential wide band model to the calculation of radiative heat transfer in one- and two-dimensional enclosures, Int. J. Heat Mass Transf. 45 (2002) 2129–2139. https://doi.org/10.1016/S0017-9310(01)00311-8.

[55] M. Bahador, B. Sundén, in: Proceeding of V Conference of Radiative Heat Transfer-IV, in: 2004: pp. 563–571. https://doi.org/10.1615/ICHMT.2004.RAD-4.

[56] M.F. Modest, H. Zhang, The Full-Spectrum Correlated-k Distribution for Thermal Radiation From Molecular Gas-Particulate Mixtures, J. Heat Transfer 124 (2001) 30–38. https://doi.org/10.1115/1.1418697.

[57] M.F. Modest, R.J. Riazzi, Assembly of full-spectrum k-distributions from a narrow-band database; effects of mixing gases, gases and nongray absorbing particles, and mixtures with nongray scatterers in nongray enclosures, J. Quant. Spectrosc. Radiat. Transf. 90 (2005) 169–189. https://doi.org/10.1016/J.JQSRT.2004.03.007.

[58] M.K. Denison, B.W. Webb, A Spectral Line-Based Weighted-Sum-of-Gray-Gases Model for Arbitrary RTE Solvers, J. Heat Transfer 115 (1993) 1004–1012. https://doi.org/10.1115/1.2911354.

[59] V.P. Solovjov, B.W. Webb, Global Spectral Methods in Gas Radiation: The Exact Limit of the SLW Model and Its Relationship to the ADF and FSK Methods, J. Heat Transfer 133 (2011) 042701. https://doi.org/10.1115/1.4002775.

[60] P. Rivière, A. Soufiani, M.Y. Perrin, H. Riad, A. Gleizes, Air mixture radiative property modelling in the temperature range 10,000–40,000 K, J. Quant. Spectrosc. Radiat. Transf. 56 (1996) 29–45. https://doi.org/10.1016/0022-4073(96)00033-7.

[61] V.P. Solovjov, B.W. Webb, SLW modeling of radiative transfer in multicomponent gas mixtures, J. Quant. Spectrosc. Radiat. Transf. 65 (2000) 655–672. https://doi.org/10.1016/S0022-4073(99)00133-8.

[62] W. Malkmus, Random Lorentz Band Model with Exponential-Tailed S-1 Line-Intensity Distribution Function, J. Opt. Soc. Am. 57 (1967) 323–329. https://doi.org/10.1364/JOSA.57.000323.

[63] S.A. Tashkun, V.I. Perevalov, CDSD-4000: High-resolution, high-temperature carbon

dioxide spectroscopic databank, J. Quant. Spectrosc. Radiat. Transf. 112 (2011) 1403–1410. https://doi.org/10.1016/J.JQSRT.2011.03.005.

[64] S.J. Young, Nonisothermal band model theory, J. Quant. Spectrosc. Radiat. Transf. 18 (1977) 1–28. https://doi.org/10.1016/0022-4073(77)90125-X.

[65] D.W. Marquardt, An Algorithm for Least-Squares Estimation of Nonlinear Parameters, J. Soc. Ind. Appl. Math. 11 (1963) 431–441. https://doi.org/10.1137/0111030.

[66] C. Ates, O. Sen, N. Selçuk, G. Kulah, Influence of spectral particle properties on radiative heat transfer in optically thin and thick media of fluidized bed combustors, Int. J. Therm. Sci. 122 (2017) 266–280. https://doi.org/10.1016/J.IJTHERMALSCI.2017.08.023.

[67] ANSYS, ANSYS FLUENT theory guide: Release 2024 R2.

[68] C. Yin, On gas and particle radiation in pulverized fuel combustion furnaces, Appl. Energy 157 (2015) 554–561. https://doi.org/10.1016/J.APENERGY.2015.01.142.

[69] L. Ma, M. Gharebaghi, R. Porter, M. Pourkashanian, J.M. Jones, A. Williams, Modelling methods for co-fired pulverised fuel furnaces, Fuel 88 (2009) 2448–2454. https://doi.org/10.1016/J.FUEL.2009.02.030.

[70] J. Zheng, B. Liu, B. Liu, Simulation of Pulverized Coal Combustion Process Considering Turbulence-Radiation Interaction, ACS Omega 8 (2023) 12944–12954. https://doi.org/10.1021/acsomega.3c00115.

[71] E.H. Chui, P.M.J. Hughes, G.D. Raithby, Implementation of the Finite Volume Method for Calculating Radiative Transfer in a Pulverized Fuel Flame, Combust. Sci. Technol. 92 (1993) 225–242. https://doi.org/10.1080/00102209308907673.

[72] S.A. Boothroyd, A.R. Jones, A comparison of radiative characteristics for fly ash and coal, Int. J. Heat Mass Transf. 29 (1986) 1649–1654. https://doi.org/10.1016/0017-9310(86)90106-7.

[73] C. Mätzler, MATLAB Functions for Mie Scattering and Absorption, Research report No. 2002-08, Institute for Applied Physics, Bern University, 2002.

[74] P.J. Foster, C.R. Howarth, Optical constants of carbons and coals in the infrared, Carbon N. Y. 6 (1968) 719–729. https://doi.org/10.1016/0008-6223(68)90016-X.

[75] T. Gronarz, J. Schulze, M. Laemmerhold, P. Graeser, J. Gorewoda, V. Kez, M. Habermehl, M. Schiemann, J. Ströhle, B. Epple, V. Scherer, R. Kneer, Quantification of the influence of parameters determining radiative heat transfer in an oxy-fuel operated boiler, Fuel Process. Technol. 157 (2017) 76–89. https://doi.org/10.1016/J.FUPROC.2016.11.012.

[76] D.G. Goodwin, M. Mitchner, Flyash radiative properties and effects on radiative heat transfer in coal-fired systems, Int. J. Heat Mass Transf. 32 (1989) 627–638. https://doi.org/10.1016/0017-9310(89)90211-1.

[77] H. Chang, T.T. Charalampopoulos, Determination of the wavelength dependence of refractive indices of flame soot, R. Soc. 430 (1990) 577–591. https://doi.org/10.1098/rspa.1990.0107.

[78] J.P. Gorog, T.N. Adams, J.K. Brimacombe, Regenerative heat transfer in rotary kilns, Metall. Trans. B 13 (1982) 153–163. https://doi.org/10.1007/BF02664572.

[79] P. V. Barr, J.K. Brimacombe, A.P. Watkinson, A heat-transfer model for the rotary kiln: Part II. Development of the cross-section model, Metall. Trans. B 20 (1989) 403–419. https://doi.org/10.1007/BF02696992.

[80] S. Colin, F. Normann, C. Fredriksson, K. Andersson, Flame Characterization of Cofiring Gaseous and Solid Fuels in Suspensions, ACS Omega 9 (2024) 28268–28282. https://doi.org/10.1021/acsomega.4c01770.

[81] S.P.E. Forsmo, S.E. Forsmo, P.O. Samskog, B.M.T. Björkman, Mechanisms in oxidation and sintering of magnetite iron ore green pellets, Powder Technol. 183 (2008) 247–259. https://doi.org/10.1016/J.POWTEC.2007.07.032.

[82] A.P. Watkinson, J.K. Brimacombe, Limestone calcination in a rotary kiln, Metall. Trans. B 13 (1982) 369–378. https://doi.org/10.1007/BF02667752.

[83] A. Fakt, A. Gunnarsson, F. Normann, K. Andersson, Evaluating heat transfer conditions in a plasma heated rotary kiln for cement production, Submitted for pulication, 2025.

[84] W.A. Fiveland, Discrete Ordinate Methods for Radiative Heat Transfer in Isotropically and Anisotropically Scattering Media, J. Heat Transfer 109 (1987) 809–812. https://doi.org/10.1115/1.3248167.